ELECTRICAL RESISTIVITY INVESTIGATION OF PART OF MMAMABULA COAL FIELD AREA FOR STRUCTURES THAT INFLUENCE THE SUBSURFACE PLACEMENT OF THE COAL SEAMS

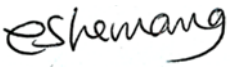
by

THATO NORAH SEANE
Reg. No: 12001368
MSc (GEOLOGY) BIUST

Earth and Environmental Science Department,
Faculty of Science,
Botswana International University of Science and Technology
thato.seane@studentmail.biust.ac.bw, (+267) 71286412

A Thesis Submitted to the Faculty of Science in Partial Fulfilment of the Requirements for the Award of the Degree of Master of Science in Geology of BIUST

Supervisor(s): Prof. Elisha M. Shemang
Earth and Environmental Science Department,
Faculty of Science, BIUST
Fax: +267 4900102 Phone Number: (+267 4900117)

Signature:  Date: 2nd November 2020

November, 2020

DECLARATION AND COPYRIGHT

I, **Thato Norah Seane**, declare that this thesis is my own original work and that it has not been presented and will not be presented to any other university for a similar or any other degree award.

Signature ……

02-11-2020

This dissertation/thesis is copyright material protected under the Berne Convention, the Copyright Act of 1999 and other international and national enactments, in that behalf, on intellectual property. It must not be reproduced by any means, in full or in part, except for short extracts in fair dealing; for researcher private study, critical scholarly review or discourse with an acknowledgement, without the written permission of the office of the Provost, on behalf of both the author and the BIUST.

CERTIFICATION

The undersigned certifies that they have read and hereby recommends for acceptance by the Faculty of Science a thesis titled: ***Electrical resistivity investigation of part of Mmamabula coal field area for structures that influence the subsurface placement of the coal seams,*** in fulfilment of the requirements for the degree of Master of Science in Geology of the BIUST.



Prof Elisha M Shemang
(Supervisor)

Date: 2nd November 2020

ACKNOWLEDGEMENT

Firstly, I would like to start by thanking my thesis advisor Prof. Elisha M. Shemang of the Faculty of Science of the Botswana International University of Science and Technology. The door to the office of Prof. Shemang was always open whenever I needed his assistance. He always made time to look through my work and steered me in the right direction. I would also like to thank my colleagues; Mr Bokani Nthaba, Ms Pabalelo Sono and our technician, Mr Boniface Kgosidintsi for their helping hand, thoughtful comments and recommendations on this thesis. Lastly, I would like to express my gratitude to my family for their unfailing support as they continuously encouraged me throughout my process of writing this thesis.

Thank you.

ABSTRACT

This study focuses on using electrical resistivity tomography (ERT) to map coal seam and associated structures found within the seams in parts of the Mmamabula Coal Field- central Botswana. The coals of this area belong to the Ecca Group' s Mmamabula Fm and Mosomane Fm. Several major faults are reported to have affected the Karoo strata in the Mmamabula area. The northern limit of the coalfields is defined by the ENE-trending Zoetfontein Fault which has a downthrow to the north of approximately 250 m. The area of study overlies the northwest-south east trending Mabuane fault. This research was undertaken in the area to determine the presence of structures (e, g faults) and how they affect subsurface placement of the coal seams in the area. Results of this study will provide relevant stakeholders with information that could be used for mine planning, mine design, environmental planning, as structural features such as faults have direct effects on coal mining. The present study was undertaken along 14 transverse lines in the area using electrical resistivity tomography survey (using the roll along-dipole dipole configuration). The results from the inversion of data obtained show a large resistivity variation within the subsurface ranging from 1.89 to 758 Ωm. From results of the resistivity the subsurface in the area was interpreted to be made of the following sedimentary units; mudstone/ shale (1.89 – 10.1 Ωm), sandstone & grit (10.1 – 20.7 Ωm), grey siltstone (28.3 – 55.1 Ωm), mudstone with thin coal (119 – 289 Ωm) and coal (289 – 758 Ωm). The subsurface placement of the coal seam as identified from the inversion models is variable; ranging from a depth 5-11 m in the NE side and 37- 46m in the SW side. The fault throw (vertical displacement) affecting the coal seams (as deduced from the interpreted resistivity sections) is approximately 32-35m. From the models it can also be concluded that the faulting is post coal deposition as the coal beds have been displaced relative to one another.

Key words: Electrical resistivity tomography, coal seams, inversion

TABLE OF CONTENTS

DECLARATION AND COPYRIGHT i

CERTIFICATION ii

ACKNOWLEDGEMENT iii

ABSTRACT iv

TABLE OF CONTENTS v

LIST OF TABLES vii

LIST OF FIGURES viii

CHAPTER 1: INTRODUCTION 1

1.1 Background Information 1

1.2 Literature review 3

1.3 Problem Statement 4

1.4 Justification of the study 4

1.5 Aim and Objectives 4

CHAPTER 2: STUDY AREA 5

2.1 Location and General Description 5

2.2 Regional geology and coal deposits 6

2.3 Local geology and Mmamabula coal resources 9

2.4 Geologic Structures 10

2.4.1 Mabuane Fault in relation to the Mmamabula coal seams 12

2.4.2 Coal seams displacement in Mmamabula coal fields- NC and SC coalfields 13

CHAPTER 3: MATERIALS AND METHODS 16

3.1 Introduction to method 16

3.1.1 Electrical Resistivity Tomography 16

3.2 Method theory 16

3.2.1 Electrical resistivity tomography 16

3.2.2 Method configuration 19

3.3 Dipole-dipole array configuration 20

3.4 Current flow into the subsurface through the electrodes 21

3.5 Resistivity of materials 23

CHAPTER 4: DATA ACQUISITION 25

4.1 Data acquisition, processing, modelling 25

4.1.1 Instrumentation 25
4.1.2 Field Procedure 26
4.1.3 Field Procedure- ROLL ALONG 27
4.2 Data handling 29
4.2.1 Data transfer and processing 29
4.2.2 Data error sources 30
4.2.3 Data quality control and assurance 30
4.2.4 Data Interpretation 31
4.3 Data modelling 32
4.3.1 Inversion and forward modelling relationship 32
4.4 Data analysis 36
4.4.1 Forward modelling 36
CHAPTER 5: RESULTS AND INTERPRETATION 41
5.1 Results introduction 41
5.2 Two Dimension Resistivity models 42
5.3 Three-dimensional resistivity models 58
CHAPTER 6- DISCUSSION AND CONCLUSION 62
6.1 Discussion 62
6.2 Conclusion 65
REFERENCES 67

LIST OF TABLES

Table 2. 1: Succession of the lithostratigraphy of the Karoo sequence by Smith (1984).....6
Table 2. 2: Summary of in situ coal resources in Botswana modified from Clark et al. (1986) as cited in Bennett (1989).....9
Table 2. 3: Summary of the in-situ coal resources in the central block of Mmamabula adopted from Robert (1999).....9
Table 3. 1: Summary of the two dimension resistivity configurations and survey characteristics; stars are in order of efficacy (four stars: most effective, one star: least effective) (modified from Loke (2014) as cited in Al-amoush et al.(2017)…….....21

LIST OF FIGURES

Figure 2. 1; Map of the location of the study area adopted from Barbolini (2010) showing the distribution of Karoo Supergroup in Botswana. 5
Figure 2. 2: Location of Botswana coal resources modified from Segwabe (2009).....8
Figure 2. 3: (a) Geological-tectonic map of eastern Botswana modified from Williamson (1996) showing the study area in relation to the fault of interest (the Mabuane fault) (b)larger view of the study area, (c) Goggle earth image showing the survey lines(Red lines indicate survey lines acquired from 07 August 2019 to 12 August 2020 and the green lines acquired from 05 February 2020 to 10 February 2020). 11
Figure 2. 4 (a): Cross section AA showing strata displacement as a result of Mabuane faulting modified from Green (1961). (b) Borehole log (B55) of Mmamabula coal field extracted from the cross section (AA). The coal seams are found within the Mmamabula and Mosomane Formations 14

Figure 3. 1: Illustration of the relationship between Resistivity and resistance through a wire.....17
Figure 3. 2: Current and potential electrodes arrangement adopted from Andrade et al.(2016) 18
Figure 3. 3: Schematic Diagram of Dipole-dipole Configuration adopted from Samanlangi (2018). 19
Figure 3. 4: Schematic Diagram of Dipole-dipole Configuration showing the relationship between the dipole pairs and the depth of penetration adopted from Samanlangi (2018)..21
Figure 3. 5:(a) Flow of current and equipotential surfaces modelled for a homogeneous subsurface (b) Flow of current and equipotential surfaces in an inhomogeneous subsurface structure; boundary z=5m. The upper layer has resistivity greater than that of the lower layer; adopted from Herman (2001) (the arrows represent the current flow, the lines indicate the equipotential surfaces).....21
Figure 3. 6: Current penetration through a heterogeneous subsurface. Blue colour represents material with low resistance (conductive medium), orange colour represents material with high resistance. (A) the electric current flow path is concentrated in the shallow depth comprising of a conductive medium, with less flow on the underlying resistive layer. (B) the flow of current is drawn to the base of the model comprising of the more conductive layer (C) the current flow lines are concentrated on the model centre where they is a conductive material (D) the current flow lines diverge away from the centre where they is a resistive material anomaly (adopted from Basin et al. (2012)).....22
Figure 3. 7: Schematic diagram showing different depth of penetration in relation to current electrode spacing adopted from Schmidt (2008). (a) closely spaced electrodes, current penetrates shallow depths, (b) widely spaced electrodes, current penetrates deeper depths. 23
Figure 3. 8: Electrical conductivity and resistivity ranges of common earth materials retrieved from Palacky (1988) 24

Figure 4. 1: Field photographs showing acquisition equipment used, comprising (a) the Syscal Pro switch unit and a battery (b) connector box connecting imaging cables (c) steel electrode connected to the imaging cable by a connecting wire 25
Figure 4. 2:(a) Schematic layout of the roll-along technique using four electrode cables (modified from Overmeeren and Ritsema (1988) as cited in Aizebeokhai (2010)), (b)Schematic diagram of the roll along method adopted from Iris Instruments (2005), segment a shifted after the standard sequence measurements to extend the system length, ...28
Figure 4. 3: Diagram showing the roll along technique as used in this survey showing measurements for the standard sequence (far left), followed by the roll along configuration. The maximum depth reached for the roll along configuration which ensured continuity in the bottom part is ¾ the maximum depth of the standard sequence. 29
Figure 4. 4: RMS error modification using error distribution bar for line 9. (a) Error distribution bar showing the cut off line. Data points with higher errors are in the right side of green cut-off line (b) Error distribution points showing the modification done using the cut off line. Red points represent bad excluded points 31
Figure 4. 5: Flow chart showing the relationship between data inversion and forward modelling adopted from Basin et al.(2012). 33
Figure 4. 6: Model blocks with data points plotted from line 4 plotted by Res2DINV, the x-axis represent the electrodes covering a distance of 720m, the y-axis represent the pseudodepth. The cross hair (x) represents the data points.....34
Figure 4. 7: Forward model simulating a fault structure in the study area. This model is made up of layers of varying thicknesses and resistivities. The shallow depths comprise of a low resistivity layer with an interbedded medium low resistivity layer. Underlying the low resistivity layer are the high resistivity layers representing coals of different resistivity values. The different resistivity shows a disturbed lateral continuity of the coal seams due to the inferred fault structure. 37
Figure 4. 8: Image of the results obtained after the inversion of the forward model (fig. 4.8), an idealized subsurface condition simulating a fault structure, (a) the measured apparent resistivity pseudosection, (b) the calculated apparent resistivity pseudosection, and (c) the inverse model resistivity section 39
Figure 4. 9: The subsurface resistivity inversion results of the field data for a profile situated at y=450 m showing, (a) the measured apparent resistivity pseudosection, (b) the calculated apparent resistivity pseudosection, and (c) the inverse model resistivity section with an absolute error of 10.0 %. The y-axis show elevation/depth and the x-axis give the distance along the profile, all in meters 40

Figure 5. 1: Resistivity section along line 1 situated at y=0 m. 42
Figure 5. 2: Resistivity section along line 2 situated at y=50 m. 43
Figure 5. 3: Resistivity section along line 3 situated at y=100 m. 44
Figure 5. 4: Resistivity section along line 4 situated at y=150 m. 46

Figure 5. 5: Resistivity section along line 5 situated at y=250 m. 47
Figure 5. 6: Resistivity section along line 6 situated at y=300 m. 48
Figure 5. 7: Resistivity section along line 7 situated at y=350 m. 49
Figure 5. 8: Resistivity section along line 8 situated at. y=400 m. 50
Figure 5. 9: Resistivity section along line 9 situated at y=450 m. 52
Figure 5. 10: Resistivity section along line 10 situated at y=500 m. 53
Figure 5. 11: Resistivity section along line 11 situated at y=550 m. 54
Figure 5. 12: Resistivity section along line 12 situated at y=600 m. 55
Figure 5. 13: Resistivity section along line 13 situated at y=650 m. 56
Figure 5. 14: Resistivity section along line 14 situated at y=700 m. 57
Figure 5. 15: Shows the inversion results (10.9% Root Mean Square) obtained using the Resistivity three dimension inversion (Res3DInv) program.....59
Figure 5. 16: Shows the 3D results in the form of vertical slices obtained also from the inversions carried out using the Res3DInv program.....61

CHAPTER 1: INTRODUCTION

1.1 Background Information

Electrical resistivity tomography (ERT) is an automated geo-tomography method commonly used in geological mapping. It is widely used to investigate areas with complex geology where the use of other geophysical methods such as the sounding method is constrained (Griffths & Barker, 1993). Due to its simplicity, low costs and ease of application, the method is widely used for near surface applications such as mineral exploration, hydrological explorations and civil engineering explorations (Loke, 1999). ERT has proven to be an effective tool in defining the complexity of the subsurface geology by identifying resistivity anomalies (Griffths & Barker, 1993).

The concept of the resistivity method was developed after the work of the Schlumberger brothers in the 1920s (Loke, 1999), having the convectional sounding surveys as the most common for quantitative interpretation. The challenge with the sounding surveys is that during data interpretation, the assumption made is that the subsurface comprises of horizontal layers hence assuming the resistivity changes are with depth (Ismael & Shariah, 2019) . This is a limitation as lateral changes in the resistivities of the subsurface can result in variations in the apparent resistivity values which may or are often misinterpreted as changes in the depth of the resistivity of the subsurface (Loke, 1999)

2-D and 3-D electrical surveys, are now the widely used practical techniques in the field of exploration comprising of relatively recent developed multi-electrode resistivity surveying equipment (Griffiths et al., 1990), rapid computer inversion softwares (Loke, 1999) and incorporate both the lateral and horizontal changes as they all have an effect of the apparent resistivity values.

ERT is widely used in mapping structural features such as faults (e.g., Vanneste et al., 2008 ; Gélis et al., 2010; Stěpančíkova et al., 2011; Monahan, 2013) and fractures (e.g., Hasan et al., 2019; Ramachandran et al,. 2012). Information on the structural control of an area is of paramount importance as it brings forth information essential during exploration of mineral deposits and subsequent mining, (Racic & Millis, 2006).

Structural changes are a concern in the coal mining industry as they have direct effects on the coal deposits. They affect coal seam thickness, its quality and also its placement. Structural mapping is critical for reasons of safety and economics (Kecojevic et al., 2005).

It is important to detect and map structures such as faults to mitigate the negative effects they may pose in relation to production and staff safety as mine design plans and production plans depend on the geometry of the deposit.

Faults have numerous undesirable effect in coal mining, it is a major contributing factor to production losses as it leads to an increase in expenditure associated to coal extraction. Monitoring analysis and production practices and show that the most encountered mining stress and dynamics are a result of faulting (Kong et al., 2019). Studies by Molinda & Ingram (1990) show that mining through a fault zone is usually expensive as it brings about additional costs such as cost of additional roof support and increased cost associated to equipment repair. These leads to hikes in operation cost hence decreasing profit margins.

It is important to draw up the accurate geometry of a deposit to reduce unplanned adjustments during mining which hinder optimal production (Molinda & Ingram, 1990). Delineating fault zones in hazard maps is vital for safe mine design as hazards during extraction are minimized.

As mentioned above, faulting results in the following effects on coal seams; seam displacement which is subject to the type of fault and its offset, weakened roof of underground mines, influx of impurities such as clay and other various forms of mineral matter into the coal deposit and also creation of water and gas pathways into the underground workings (Nelson, 1981).

Coal seams may be displaced by several meters vertically or horizontally depending on the type of faulting that has occurred. Dip slip faults are a great concern in open pit mining as up thrown blocks in most cases are eroded whilst downthrown blocks are at deeper depths for profitable recovery. Faulting destabilise rock structures which is a safety hazards in mine workings as roof and pillars are weakened. They also create natural pathways that can be conduit for water and gas into mine working, some gases are flammable which is a hazard while the waters can result in mine flooding. Faults also introduce impurities into the coal, the most common is clay, sand, pyrite, calcite, quartz. Such minerals increase the sulphur and ash content in the coal thereby affecting its quality and also cause accelerated mining equipment wear and tear (Nelson, 1981).

Ji et al ., 2012 stated that mining near faults triggers dynamic disasters in regions of tectonic stress concentration such as rock burst and mine earthquake. Mining near a fault can lead to changes in the tectonic stress and also the release of tectonic strain energy. The effects

include changes in the stress status in the fault and the changes in the mechanical or physical parameters of the surrounding rock mass in close proximity to the fault (as cited in Ji et al ., 2012).

High resolution geophysical methods are widely adopted in mapping of structures found in ore/mineral deposits. Van Schoor & Fourie (2014) carried out a study on " the application of geophysics in South African coal mining and exploration"; his results revealed that geophysics surveys can be used as a guide in coal mining. The results can provide caution in cases of deviations from the coal seam continuity or delineate any structural hazard which constitute to production or safety hazard.

1.2 Literature review

Several researches have been carried out that proved the efficiency of electrical resistivity tomography in the mapping of areas with complex geology. Giocoli et al., (2009) applied ERT to investigate the structural setting of the Ufita Valley. The results revealed the effectiveness of the method in imaging the active fault and revealing the geological setting of the area. From his work, he was able to map out the location and geometry (the dip, vertical displacement) of the active faults at the surface.

Torgashov et al (2010) acquired ERT data across an underground limestone mine access tunnel on the ground surface. The research was aimed at determining the cause of the rock falls and also explicate the geologic nature of the lineament. There had been so many recorded occurrences of localized failure on the ceiling of the access tunnel and other localities following a previously unknown northwest trending lineament. The results obtained indicated dissection by several protruding clay bearing near vertical solution widened joints and/or fractures on the limestone roof rock above the tunnel that are not visually exposed on the ceiling of the tunnel.

Monahan (2013) also used electrical resistivity tomography to investigate a fault structure, the results obtained from the 2D inverted resistivity profiles correlated with the geological evidence from previous drill studies. Using resistivity contrast, the method was able to distinguish sedimentary units, delineate the approximated fault location in bedrock and also estimate vertical displacement.

1.3 Problem Statement

Mmamabula area is a proposed site for near future coal exploitation. Coal investigation (i.e. the use of drilling) in the area has been focused on the coal grade and its subsurface placement with less emphasis on the structural framework of the area. Structures affect coal seam thickness, its quality and also its placement. Limited structural knowledge in the study area can result in the difficulty in future coal exploration and also result in expensive exploitation. Better understanding of coal resources and their occurrence go a long way in increasing the success rate of mining in the area.

1.4 Justification of the study

Several major faults are reported to have affected the Karoo strata in the Mmamabula area forming the major structural controls. Three main fault trends are identified; the ENE-WSW, NNW-SSE and WNW-ESE (Fig 2.3(a and b)) to have affected the greater Mmamabula coal field thereby dividing it into several structural units. With faulting in the area, there is need for a study to be undertaken in the area to determine the existing structures (e.g. faults) in the area and determine their influence in the subsurface placement of the coal seams. The identification of the presence of faults in the area and their effects on coal seam location and geometry will provide invaluable information in mine planning and design in the area in order to improve safety during mining of the coal resources in the area.

1.5 Aim and Objectives

Aim: To investigate structures in part of Mmamabula so as to understand their relationship with the subsurface placement of the coal seams.

Objectives:

- To carry out electrical resistivity tomography survey to determine the nature and type of structures and the location
- Delineate coal seam location
- To determine the relationship between the structure and the coal seam placement if any
- To provide and insight into the type of structural deformation that has occurred

CHAPTER 2: STUDY AREA

2.1 Location and General Description

The study area is about 0.468 square kilometres and lies in the South-eastern part Botswana. It is located at approximately -23.610123 latitude and 26.544874 longitude in the Mmamabula area as shown in Figure 2.1 and forms part of the explored coal resources of the Greater Mmamabula.

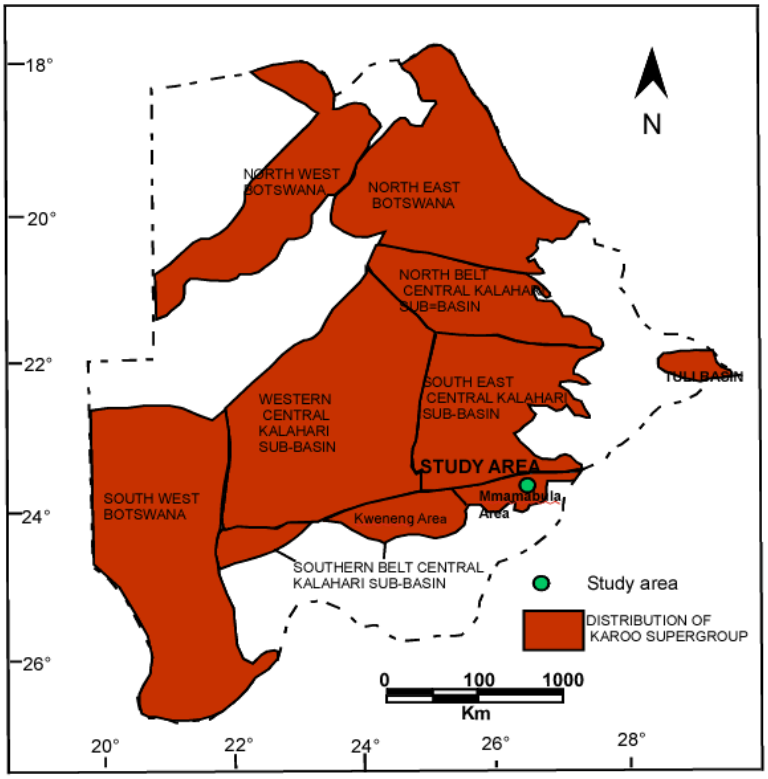


Figure 2. 1; Map of the location of the study area adopted from Barbolini (2010) showing the distribution of Karoo Supergroup in Botswana.

The area is accessible via the main tarred road, the A1 road and railway line trending south-west to the north-east from Gaborone to Francistown (and beyond). The principal economic activity is cattle grazing supplemented by small stock farming. Climate is described as semi and subtropical climate with the Tropic of Capricorn forming the northern boundary (Williamson, 1996.) The rains in the area are mostly experienced between hot summer months from November to April although some slight rains are experienced in winter months. The area is also prone to prolonged drought periods. Temperature variation is seasonal and diurnally with winter days being warm to cool on early mornings. Summer days are hot during the days and mild during the night.

2.2 Regional geology and coal deposits

The coal deposits in Botswana are hosted in rocks found in the Karoo Supergroup as described by Smith (1984). Potentially exploitable areas for coal in Botswana are found mostly in the south-western and eastern flanks of the Kalahari-Karoo basin (correlation of fig 2.1 and 2.2). Geologically the Kalahari Basin underlies at least 60% of the country (Hancox, 2016), the distribution of the Karoo is poorly exposed as they are uncomfortably overlain by the Kalahari beds (Carney et al., 1994). The distribution is controlled by the North-easterly trending faults to the west and the northwest trending faults and flexures in the eastern side of the country (Carney et al., 1994).

Stratigraphic sections for the sub-basins by Smith (1984) indicate that the Karoo sedimentary sequences in Botswana thicken to the west and south west. The increased thickness in the south west is mainly attributed from the development of the lower Karoo units (Ecca and Dwyka groups) (Bennett, 1989). The Kalahari Karoo Basin in Botswana is divided into seven sub-basin based from the geological setting related to facies changes and basement features (Smith, 1984). The succession of the lithostratigraphy of the Karoo sequence is shown in table 2.1

Table 2. 1: Succession of the lithostratigraphy of the Karoo sequence by Smith (1984)

	Group	**Formations**	
KAROO SUPERGROUP	Stomberg lava	Stomberg lava group	
	Lebung	Ntane Sandstone Fm	
		Mosolotsane Fm	
	Beaufort	Lekotsana	
		Tlhabala Fm	
	Ecca	Korotlo Fm	Sandstone, siltstone, carbonaceous mudstone, and coal Mudstone
		Dibete Fm	
		Mmamabula Fm	
		Mosomane Fm	
		Bori Fm	
	Dwyka	Dukwi Fm	

The basal unit of the Karoo Supergroup is the Dwyka group deposited during permo - carboniferous glacial events. It comprises of tillite dominated assemblage followed by

glaciofluvial sandstone and glaciolaucastrine. The Dwyka is overlain by an upward gradation into the Ecca and Beaufort Groups.

The Ecca group comprises of a varied sequences of carbonaceous shale, mudstones, siltstones and coals. It is subdivided into the lower, middle and upper Ecca Subgroups. Argillites and carbonaceous argillites form part of the Lower Ecca, episodes of volcanism and intrusions is also evidenced by dolerite sills and volcanic breccias found in the subgroup (Carney et al.,1994). The Middle Ecca Subgroup comprises of coal measures in abundance which dominate the faulted eastern margin of the Karoo Supergroup basin. Most of the coal deposits are reported to have formed in river flood plains and deltas or abandoned river channels in ancient river system (Williamson, 1996). Upper Ecca Subgroup comprise of carbonaceous mudstones and relatively bright coals that accumulated during the stabilization of the topographic irregularities after infiltration when rates of subsidence were uniform (Smith, 1984).

Overlying the Ecca group successively is the Beaufort Group, Lebung group and the uppermost Stomberg Lava group. The existence of the Beaufort Group is inferred from South African beds. Rocks from this group are considered to range between Middle Permian to Early Triassic in age. The deposition of the Tlhabala Formation (lacustrine-estuarine) resulted from climatic warming and an increase in aridity (Smith, 1984). The Lebung Group comprises of the clastic formations with ‘red beds’ affinity. The Stomberg Lava group marked the end of Karoo sedimentation by the tholeiitic flood basalts (Carney et al., 1994).

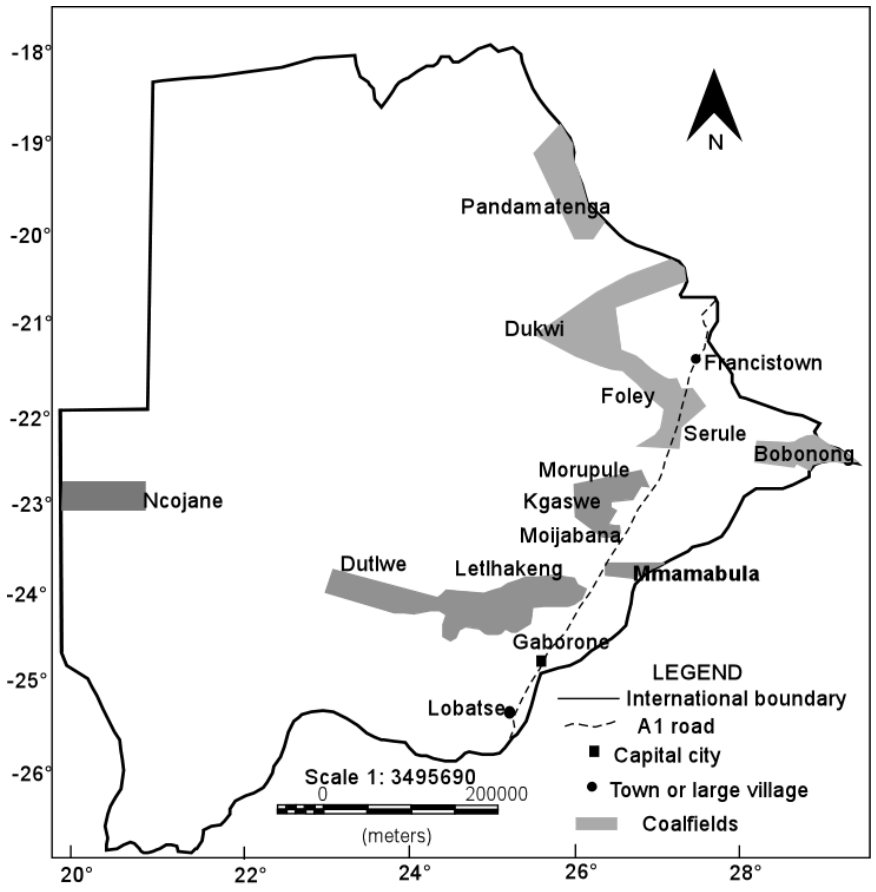


Figure 2. 2: Location of Botswana coal resources modified from Segwabe (2009)

Coal resources in Botswana are widely studied (Clark et al., 1986; Barbolini, 2010; Bennett, 1989; Carney et al., 1994). Exploration of the coal resources have confirmed in situ resources of approximately 20 000Mt of coal as shown in table 2.2. Thick better developed coal sequences are reported to occur in graben or closer to paleo-islands illustrating the over-riding of regional controls by local controls, whilst the thin coals are laterally extensive indicating deposition in relatively stable and low energy environments (Bennett, 1989). The coals are predominantly inertinite and have high ash content attributable to the bituminous type and have a medium calorific value and high inherent moisture content (Carney et al., 1994). Coal deposits in Botswana shows a probability of having many time periods of deposition and localized faulting and this is reflected by the number of sub- basins that the coal fields have been divided into as shown in figure 2.2.

Table 2. 2: Summary of in situ coal resources in Botswana modified from Clark et al.(1986) as cited in Bennett (1989).

Exploration block	Area (km2)	Total in situ resources (Mt)
Morupule	610	7 910
SW Moijabana	250	1 300
Mmamabula	800	5 175
Letlhakeng	670	3 530
Dutlwe	350	2 000
TOTAL	**2 680**	**19 915**

2.3 Local geology and Mmamabula coal resources

Mmamabula coal field is situated approximately 130km south of Morupule coal field. The coals occur in a triangular uplifted area found between the converging ENE trending Zoetfontein and NNW trending Mabuane Fault (Green, 1961).

Table 2. 3: Summary of the in-situ coal resources in the central block of Mmamabula adopted from Robert (1999).

Seam			**Lower Seam**	**Middle Seam**	**Upper Seam**
Average thickness (m)			2.83	5.39	2.07
Average S.G.			1.5	1.54	1.67
In -situ Tonnage (Kilotons)			159 251	212 7769	70 923
Raw	Ash	%	19.5	20.8	34.2
	Volatiles	%	25.1	25	24.1
	GCV	(MJ/kg)	25.1	23.95	18.94
	Sulphur	%	2.08	1.68	2.19
	Ash	%			
Washed	Yield	%	80	46.06	30
Cum float	SG		1.6	1.5	1.5
	Ash	%	13.3	11.4	10.1
	Volatiles	%	27.3	27	32.8
	GCV	(MJ/kg)	37.35	27.76	28.24
	Sulphur	%	0.44	0.41	0.42

Three important coal seams of possible economic interest are found in Mmamabula and are restricted to the Ecca group as shown in table 2.1 within the Mmamabula and Mosomane Fm (Robert, 1999). The lowest of the three seams ‘the lower seam’ is found within the

Mosomane Fm; it has an average thickness of 2.83m and is found at a depth below surface from 30m to 60m in the west area of sub-outcrop. The seam comprises of mixed bright banded coals with minor shale bands locally (Robert, 1999).

The base of Mmamabula Fm comprises of the middle coal seam which is separated from the lower seam by 17 -18m of thin mudstone, feldspathic and gritty sandstone. The seam has an average thickness of 5.39m and extends over an area of about 32km^2 (Robert, 1999). The middle seam is thought to correlate with the Morupule main seam (Bennett, 1989). It is inferior in quality to the lower seam due to the presence of thin bands of carbonaceous shale within it; some with an average thickness of 0.5m.

Above the middle coal seam at approximately 10m lies the 'Upper coal seam' that comprise of bright coal. It has an average thickness of 2.07m, with a restricted coverage of 5km^2. The upper coal seam has the poorest quality compared to the other seams as it is intercalated with carbonaceous shale bands (Robert, 1999; Green, 1961).

Figure 2.4 (b) shows a detailed information on the lithological borehole log B55 used as a reference borehole to explain in detail the lithological relationship of the study area. The Ash content of three seams ranges approximately from 19.5 to 34.2 percent, calorific value from 25.10 to 18.94 MJ/kg, Sulphur ranges from 1.68 to 2.19 percent (Bennett, 1989), as shown in table 2.3.

2.4 Geologic Structures

The study area forms part of the Greater Mmamabula coal field situated along the Kalahari Karoo Basin south eastern margins. It is contiguous with the Waterberg coal field found in South Africa. Faults form the major structural controls of the area with their traces shown from a number of interpreted satellite imagery, aeromagnetic data and borehole data. There are three main fault trends identified that include the ENE- WSW, NNW-SSE and WNW-ESE (Fig 2.3(a and b)) that have affected the greater Mmamabula coal field thereby dividing it into different structural units.

The most prominent fault in the entire Greater Mmamabula coalfield is the Zoetfontein Fault, forming the Northern limit of the Eastern Mmamabula coal field, it is the most prominent feature in the area causing ENE-WSW displacements with a downthrow to the north of at least 250 metres (Robert, 1999; Bennett, 1989). Green (1966) considered the possibility that Ecca group sedimentation in the Central and Eastern Mmamabula Coalfields

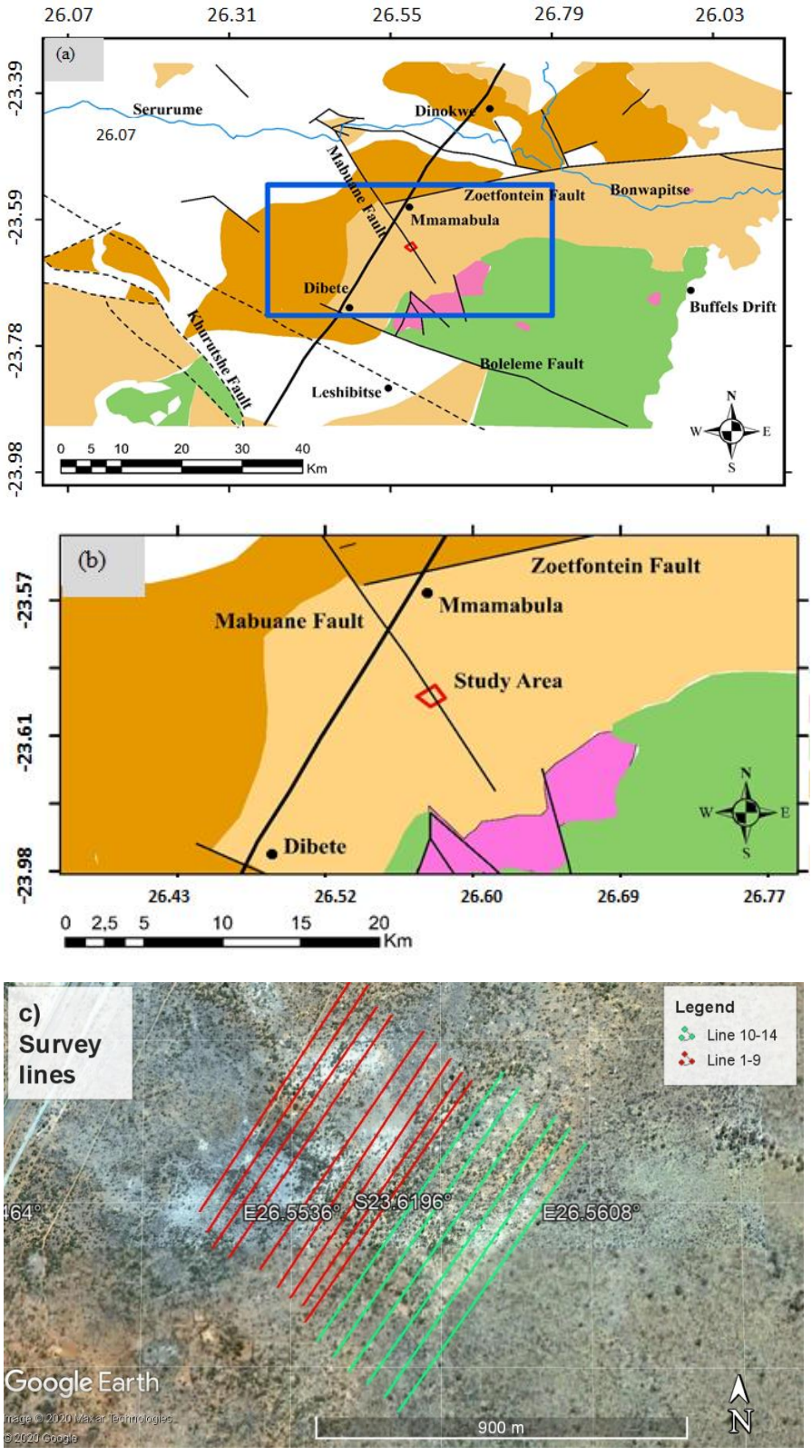


Figure 2. 3: (a) Geological-tectonic map of eastern Botswana modified from Williamson (1996) showing the study area in relation to the fault of interest (the Mabuane fault) (b)larger view of the study area, (c) Goggle earth image showing the survey lines(Red lines indicate survey lines acquired from 07 August 2019 to 12 August 2020 and the green lines acquired from 05 February 2020 to 10 February 2020).

was controlled by the Zoetfontein fault. Several faults trend subparallel to the Zoetfontein Fault, they include the Southern Boundary fault, Maphashakeka-Ellofsdale Fault and the Mookane fault which separates the Ecca and Dwyka Group sequences.

The NNW-SSE trending Khurutshe Fault is another prominent fault forming the eastern margin of the Western Mmamabula Coal Field. It trends parallel to and is inferred to be bounded on its south-western side at depth by the Pilanesburg dyke swarm and there is a possibility that it was active prior deposition of Karoo Super group.

Structure forming the WNW-ESE trends include the Boleleme Fault that forms the northern margin to the Southern Mmamabula Coal field and the southern margin to the South central coal field. It is also reported to have played a major role in controlling the Ecca group sedimentation in the South Central coalfields.

2.4.1 Mabuane Fault in relation to the Mmamabula coal seams

The area of study overlies the northwest-south east trending Mabuane fault. The ERT survey lines are as indicated in fig 2.3(c) cutting across the Mabuane fault covering both the north-central (NC) and south central (SC) coal fields from the Greater Mmamabula coal fields. The North-central coal field is bounded to the north by the Zoetfontein fault and to the west by the Mabuane Fault. The Mabuane fault is a down throw fault to the south west that separates the South- central coal field from the North-central coal field (Williamson, 1996).

According to Robert (1999), the two coal fields of interest; the South-central and North-central have similar stratigraphic units with three major coal seams; the M1 (lower seam) and the M2 (middle and upper seams). The M1 seam is found at greater depths. In the North-central coal field its thickness is averaged between 2m and 4 m characterized by a mix of bright and dull coals. In the South-central coalfield the seam has an averaged thickness between 2.5m to 4.3m (Williamson, 1996).

The M2 seam comprise of 2 major coal (middle and upper seams) intervals separated by a sequence of interbedded coals, carbonaceous mudstone and coaly mudstones (Smith, 1984). The ‘middle seam’ in the NC coalfield has a thickness between 4.8m to 6.2m averaged 5.4m with high quality coals found at the base of the seam. The ‘middle seam’ in the SC coalfield is also of good quality coal from basal portions and deteriorating upward averaging 5.7m in thickness (Williamson, 1996).

The M2 ‘upper seam’ in the NC coalfield is separated from the M2 ‘middle seam’ by an 8m to 10 m thick sequence of interbedded black shales, carbonaceous, claystone and coals. The seam is averaged 2.1 m in thickness and is characterized by coals with bands of mudstone and carbonaceous shale. This seam is overlain by up to 4m interbedded massive carbonaceous mudstone (Williamson, 1996). The South-central M2 ‘upper seam’ coal has an average thickness of 1m and is overlain by mudstone and separated from the ‘middle seam’ by approximately 6m to 9m of carbonaceous mudstones and thin coals (Smith, 1984; Williamson, 1996).

2.4.2 Coal seams displacement in Mmamabula coal fields- NC and SC coalfields

As stated above the Mabuane fault is a down thrown fault to the south west. The South-central coal field strata are downthrown to greater depths thus affecting coal seam placement. The relationship between the two central coal fields is shown in fig.2.4(a).

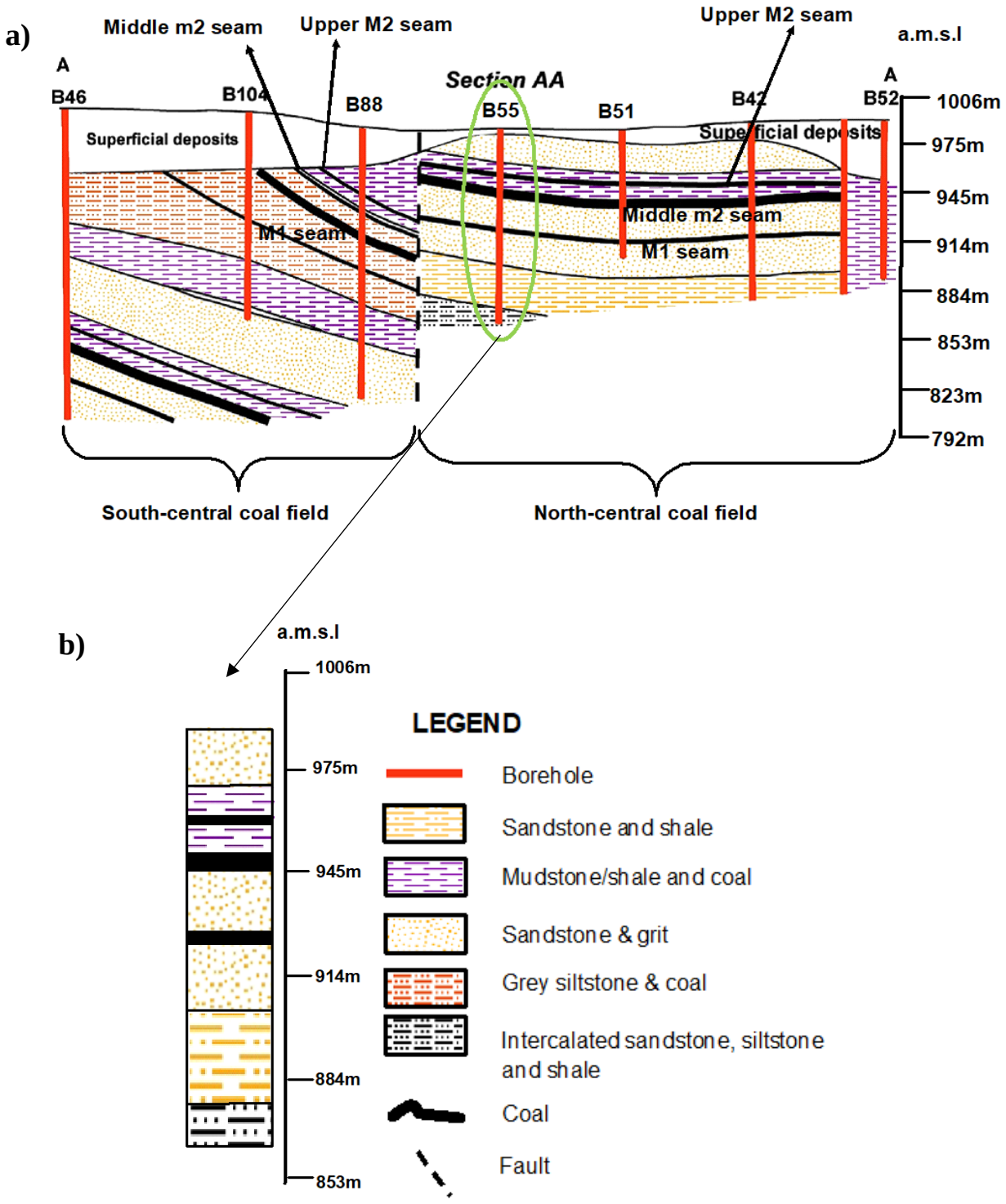


Figure 2. 4 (a): Cross section AA showing strata displacement as a result of Mabuane faulting modified from Green (1961). (b) Borehole log (B55) of Mmamabula coal field extracted from the cross section (AA). The coal seams are found within the Mmamabula and Mosomane Formations

Williamson (1996) supported the findings by Green (1961) that seam displacement resulting from the Mabuane faulting had occurred in the Greater Mmamabula coal seams (see Figure

2.4(a). Studies on the coal resources in the Greater Mmamabula indicated that the coal quality is fairly consistent in the area with subtle decrease in ash content from the north to the south (Williamson, 1996). Suggate (1974) indicated that the coal quality is a function of the depth of its placement, and thus concluded that deep seated coals have higher quality as a result of burial depth pressures.

CHAPTER 3: MATERIALS AND METHODS

3.1 Introduction to method

The method approach for this study commenced with desktop studies which included topographic maps, satellite data and available literature of the study area. Pre-existing work was assessed to understand the current research area and also to identify gaps to fill hence supplement the already available documentation. The main method adopted for this research is electrical resistivity tomography. The data obtained was analysed to determine the relationship between any geological structures and the coal seams in the study area.

3.1.1 Electrical Resistivity Tomography

Electrical resistivity Tomography (ERT) is a geophysical exploration technique widely used in the imaging of subsurface structures. It measures electric potential differences at specific locations resulting from controlled current injection in other places (Basin et al., 2012). The method uses the variations in the resistivity of the subsurface to generate 2D and 3D high resolution images (Giocoli et al., 2009). Due to its high resolution it is considered suitable for fracture identification (Qarqori et al., 2012).

ERT method is widely used in solving geological problems such as determining the position of active faults, quantifying displacements in Quaternary formations (Diaferia et al., 2006; Giocoli et al., 2009) and also investigation of coal resources (Omowumi et al., 2018). The method is also useful in clayey ground by defining transitional boundaries that are difficult to detect by other geophysical methods (Iungu, 2015).

Modelling of the data obtained using electrical resistivity tomography is performed through carrying out an inversion, a procedure for processing geophysical data. Inversion computing is both complex and intense, it uses variation in resistivity to creates two-dimensional or 3-dimentional vertical cross sections beneath the electrode array (Loke, 2001).

The results of inversion are presented as pseudosections (also called pseudodepth section or a quasi-section); a diagram presenting a plot of the data points along the transverse lines. It shows the resistivity distribution as a function of location and depth.

3.2 Method theory

3.2.1 Electrical resistivity tomography

Electrical resistivity, a mathematical inverse of conductivity is a bulk physical property of a material that obstructs current flow (Nur Amalina et al., 2017). It is expressed as the

resistance through unit distance and the SI units are in ohm-meters (Monahan, 2013). The imaging technique is based on the Ohm's Law, equation 3.1 which describes the flow of electric current through a resistive material. The law relates electric current (I) passing through a resistor to the voltage (V) applied across the resistor and its conductance (R) (Basin et al., 2012). The law states that the electrical current through a material is directly proportional to the potential difference (ΔV) across it (Loke, 2001).

$$I = \frac{V}{R} \quad \text{..... (3.1)}$$

Resistance (R) is also directly proportional to the conducting material length, L and inversely proportional to the cross-sectional area A (equation 3.2), with the constant of proportionality being the resistivity

$$R = \rho \frac{L}{A} \quad \text{..... (3.2)}$$

Electrical resistance is the opposition of electric current flow through a defined volume of any material given. Figure 3.1 is an illustration of the relationship between resistivity and resistance. The resistivity value of any material is tied to the material composition. For instance, a copper wire would have a specific resistivity value and its resistance would be a function of the thickness and length of the wire.

Resistivity vs Resistance

$\rho = R\frac{A}{L}$ $\quad$ $R = \rho\frac{A}{L}$

Where;

ρ : resistivity of the wire material

A: cross sectional area

R: resistance of wire

L: length of wire

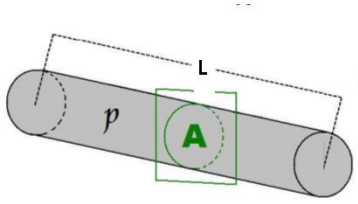


Figure 3. 1: Illustration of the relationship between Resistivity and resistance through a wire.

To acquire resistivity measurements of a cross-section of the earth, electrodes pairs (A and B) are used as current (I) injectors into the ground and the potential drop (V) is acquired by two other electrodes (M and N) (see fig 3.2) (Giocoli et al., 2009). Resistivity data is recorded through a complex pairing combinations of current and potential electrodes. The combinations result in a pseudo cross-section of apparent resistivity constructed

beneath the survey line (Dahlin & Zhou, 2006). The electrodes are usually arranged in a linear array as shown in fig 3.2.

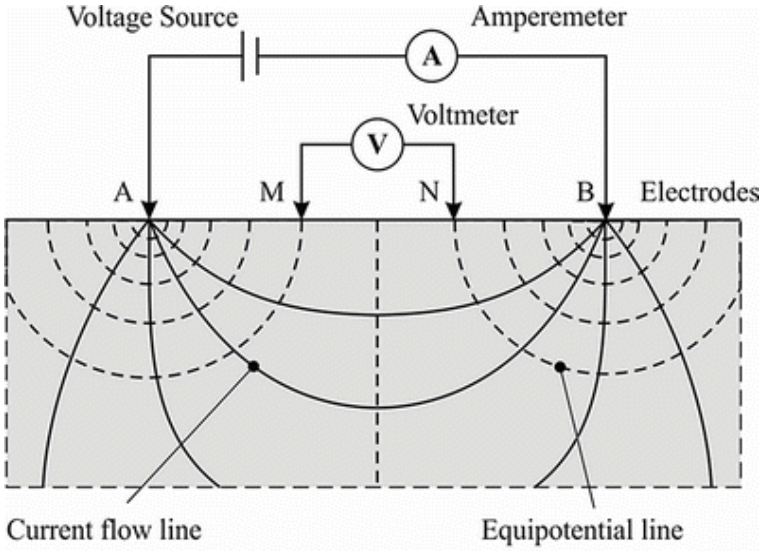


Figure 3. 2: Current and potential electrodes arrangement adopted from Andrade et al.(2016)

As current travels through the ground, it encounters zones with different resistivity values. Any acquired value of resistivity is referred to as apparent resistivity (ρa) as it is not the true resistivity of the layers but a function of the in-homogeneities (Schmidt, 2008). A formula applicable to the electrode configuration deployed is used to compute the apparent resistivity from the resistance measurements (Lowrie, 2007). The apparent resistivity is then a function of the impedance measured (potential to current ratio) and of the electrode array geometry (Schmidt, 2008).

From fig. 3.2, electrode A and B represent the current source and the current sink respectively. Voltage is measured across the potential electrodes M and N. Thus if electrode A carries current I. The potential drop at M is calculated as;

$$V = \frac{Il\rho}{A} \quad \text{(3.3)}$$

where l is the distance from the electrode, ρ resistivity A is the area of the cross section.

Assuming that current distribution is uniform over half- sphere;

$$V = \frac{Il\rho}{A} = \frac{Ir\rho}{2\pi r^2} = \frac{I\rho}{2\pi r} \quad \text{(3.4)}$$

Potential drop at M and N is calculated as: (contributions for each are from electrodes A&B);

$V_M = \frac{I\rho}{2\pi}[\frac{1}{AM} - \frac{1}{MB}]$……. (3.5)

$V_N = \frac{I\rho}{2\pi}[\frac{1}{AM} - \frac{1}{MB}]$…….. (3.6)

where AM and MB represent the distances from the point to electrodes A and electrode B

Between N & M electrodes the potential difference is calculated as;

$\Delta V_{NM} = \frac{I\rho}{2\pi}[\frac{1}{AN} - \frac{1}{AM} - \frac{1}{MB} + \frac{1}{NB}]$…… (3.7)

Rearranging results in; $\rho = \frac{2\pi\Delta VNM}{I}\ [\frac{1}{AN} - \frac{1}{AM} - \frac{1}{MB} + \frac{1}{NB}]^{-1}$

Hence $\rho = \frac{\Delta V}{I}k$……(3.8)

K is a geometric factor whose value depends on the type of array configuration used. The array type used in these survey is dipole-dipole (fig 3.3). Hence;

k = (πn(n+1) (n+2) a) …… (3.9)

The mathematical demonstration for deriving the equation is given by (Herman, 2001)

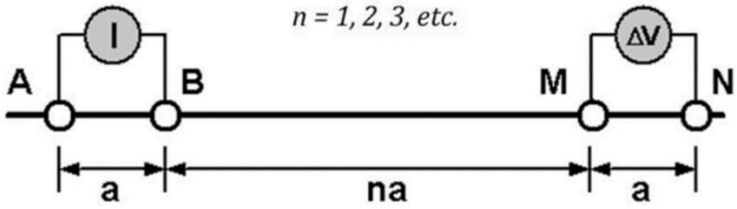


Figure 3. 3: Schematic Diagram of Dipole-dipole Configuration adopted from Samanlangi (2018).

3.2.2 Method configuration

In carrying out data acquisition, four electrodes are normally placed at arbitrary positions. There are a number of common arrays used and the choice of array type to use depends on the nature of the geological structure of interest to be delineated, subsurface heterogeneities, resistivity meter sensitivity, electromagnetic coupling and background noise level (Aizebeokhai, 2010). Other factors considered include the array sensitivity to horizontal and vertical changes in the resistivity of the subsurface, maximum depth of investigation, signal

strength and horizontal data coverage (Al-amoush et al., 2017). Table 3.1 is a summary of the most widely used configurations and their strengths.

Table 3. 1: Summary of the two dimension resistivity configurations and survey characteristics; stars are in order of efficacy (four stars: most effective, one star: least effective) (modified from Loke (2014) as cited in Al-amoush et al. (2017)

Configuration/ Characteristics	Dipole-Dipole (DD)	Wenner-Schlumberger(WS)	Wenner(W)
Sensitivity of the array to horizontal structures	*	**	****
Sensitivity of the arrray to vertical structures	****	**	*
Depth of investigation	***	**	*
Horizontal data coverage	***	**	*
Signal strength	*	***	****

The dipole-dipole is considered to be the most sensitive to horizontal variations and comparatively less sensitive to vertical subsurface variations (Al-amoush et al., 2017). It is widely used in the mapping of vertical structurs such as faults, cavities and dykes and. It is poor in mapping horizontal structures such as sills or sedimentary strata (Loke, 2000). Wenner-Schlumberger and Wenner arrays have stronger signal strength and moderate depth of investigation. They are better suited in resolving vertical changes and poor in detecting horizontal changes (Al-amoush et al., 2017).

3.3 Dipole-dipole array configuration

Dipole-dipole array was used in this study, the convention is to maintain a constant separation distance between the dipole pairs (current electrodes and the potential electrodes). The distance is maintained as an integer multiple of the current and potential electrode spacing (Monahan, 2013). When taking measurements, the spacing between A-B electrodes and that between the M-N electrodes usually starts at ‘1a’.

The first set of measurements are made with 1 as the value of ‘n’. The next set is acquired by gradually increasing the value of ‘n’ whilst keeping the A-B dipole pair fixed at ‘1a’. Six

is usually considered as the maximum "n" spacing factor that still gives better resolution results. The depth of investigation is increased by increasing the spacing between the A-B dipole pair to '2a', the value of 'n' is also changed when acquiring a further series of readings (Loke, 2000). Fig 3.4 shows a schematic layout of the dipole-dipole configuration.

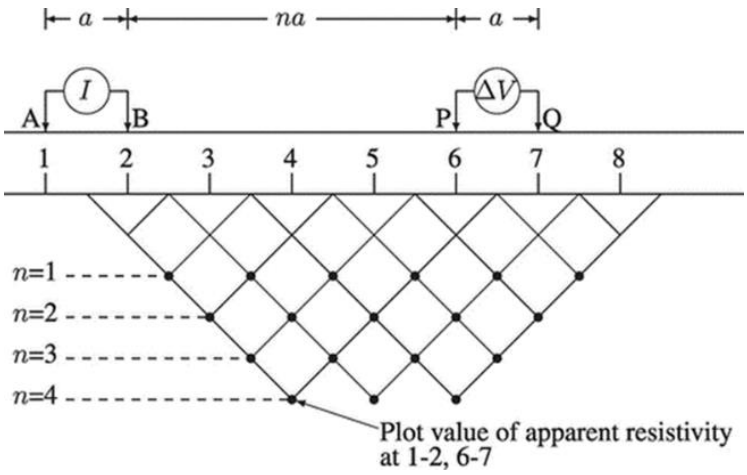


Figure 3. 4: Schematic Diagram of Dipole-dipole Configuration showing the relationship between the dipole pairs and the depth of penetration adopted from Samanlangi (2018)

3.4 Current flow into the subsurface through the electrodes

When an electrical current is introduced into a homogeneous ground (fig 3.5a), it spreads uniformly across a hemispherical shell centered on the source to define an equipotential surface (Schmidt, 2008). Equipotential surfaces are perpendicular to current lines, they create local ''volt-drops'' which according to Ohms law; I=V/R (Herman, 2001).

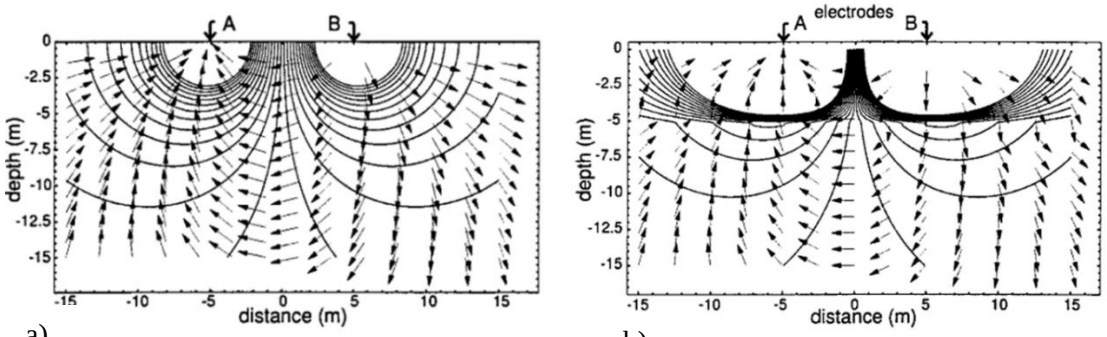


Figure 3. 5:(a) Flow of current and equipotential surfaces modelled for a homogeneous subsurface (b) Flow of current and equipotential surfaces in an inhomogeneous subsurface structure; boundary z=5m. The upper layer has resistivity greater than that of the lower layer; adopted from Herman (2001) (the arrows represent the current flow, the lines indicate the equipotential surfaces)

Electric current injected into the ground follows a path with less resistance and concentrates in areas of conductive material. The illustration on how the flow of current is affected by subsurface heterogeneities is shown in figure 3.6.

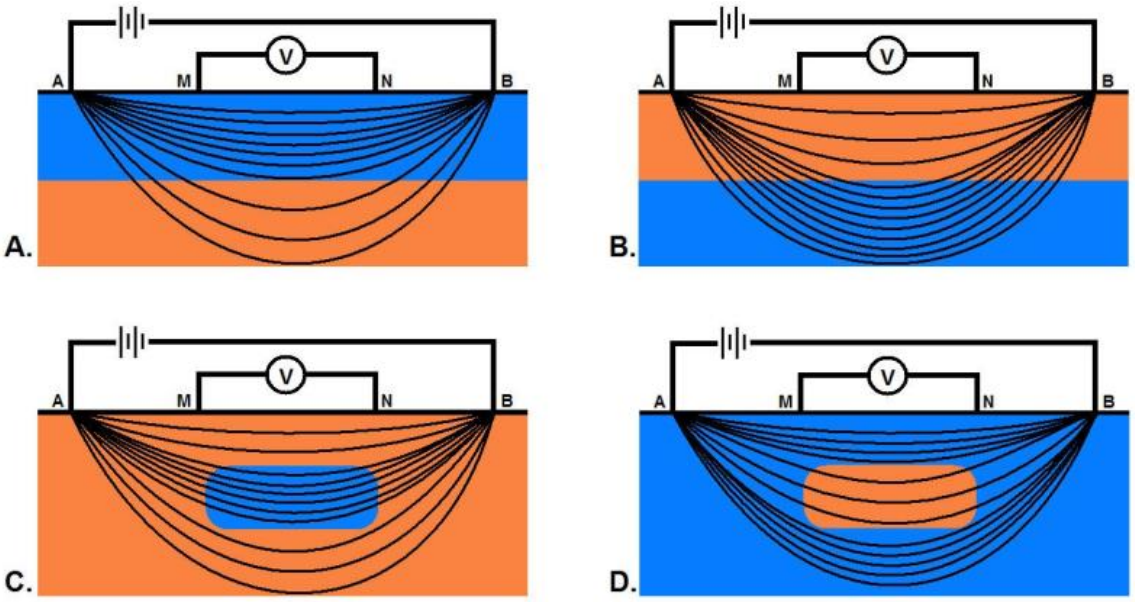


Figure 3. 6: Current penetration through a heterogeneous subsurface. Blue colour represents material with low resistance (conductive medium), orange colour represents material with high resistance. (A) the electric current flow path is concentrated in the shallow depth comprising of a conductive medium, with less flow on the underlying resistive layer. (B) the flow of current is drawn to the base of the model comprising of the more conductive layer (C) the current flow lines are concentrated on the model centre where they is a conductive material (D) the current flow lines diverge away from the centre where they is a resistive material anomaly (adopted from Basin et al. (2012))

For a heterogeneous ground, current does not travel uniformly. Fig 3.5(b) illustrates the current flow in a medium where the upper layer constitutes of material with higher resistivity than the layer below. The equipotential surfaces are further apart in the low resistivity layer compared to the high resistivity top layer. Current penetrating through different materials alters its course through the materials accordingly, these alteration between the electrodes forms the basis to depict a boundary between the two layers (Herman, 2001).

The penetration depth is increased by increasing the separation between the two current electrodes (Schmidt, 2008). The resistance encountered by the current between the electrodes is primarily that of the material at a depth that is less than several times the

spacing of the current electrodes (Herman, 2001). Acquiring resistivity values at different depth is achieved by increasing or decreasing the electrodes separation (fig 3(7)).

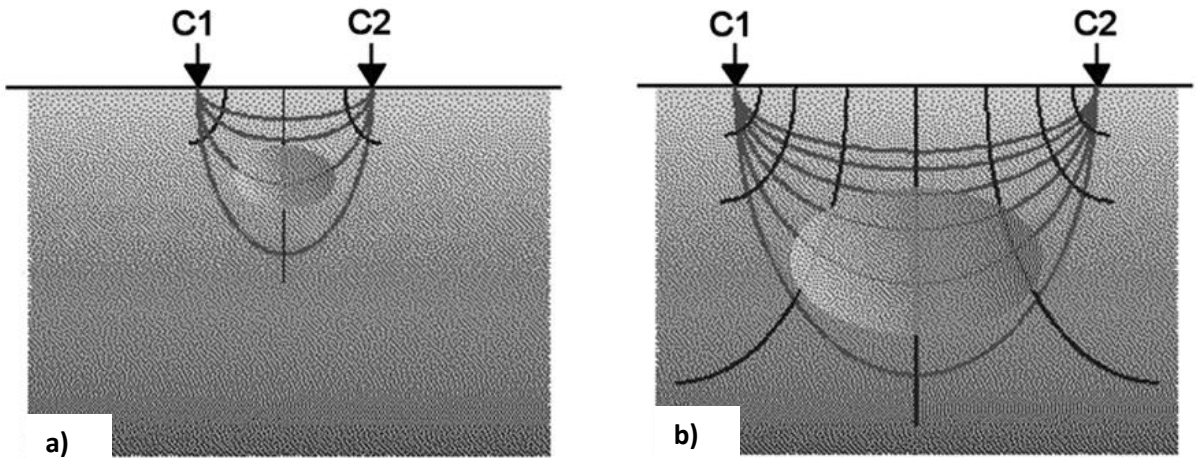


Figure 3. 7: Schematic diagram showing different depth of penetration in relation to current electrode spacing adopted from Schmidt (2008). (a) closely spaced electrodes, current penetrates shallow depths, (b) widely spaced electrodes, current penetrates deeper depths.

3.5 Resistivity of materials

Subsurface materials have variable resistivity values due to their nature and type. Because most rocks are poor conductors, current travels through the process of electrolytic conduction in which the propagation of current is by ionic conduction. Rocks are usually porous and have water filled pores hence act as electrolytic conductors. Their resistivities vary with the mobility, degree of dissociation and concentration of the ions (Keller, 2017).

Sedimentary rocks tend to have lower resistivity values than Igneous and Metamorphic rocks. The sedimentary rocks have low resistivity values as they are more porous and usually have water filled voids (Loke,2000). Resistivity values of igneous and metamorphic correlate to their degree of fracturing and the percentage of the infilled ground water. Due to this variations, measuring the resistivity of an unknown material can be useful in identifying that material, combined with geologic information it can be used in constituting the various underground layers (Herman, 2001).

Resistivity values overlap is common in the different classes of rocks and soils as it is influenced by a number of factors that include porosity, concentration of dissolved salts and the degree of water saturation. Fig 3.8 shows the electrical conductivity and resistivity ranges of common earth materials.

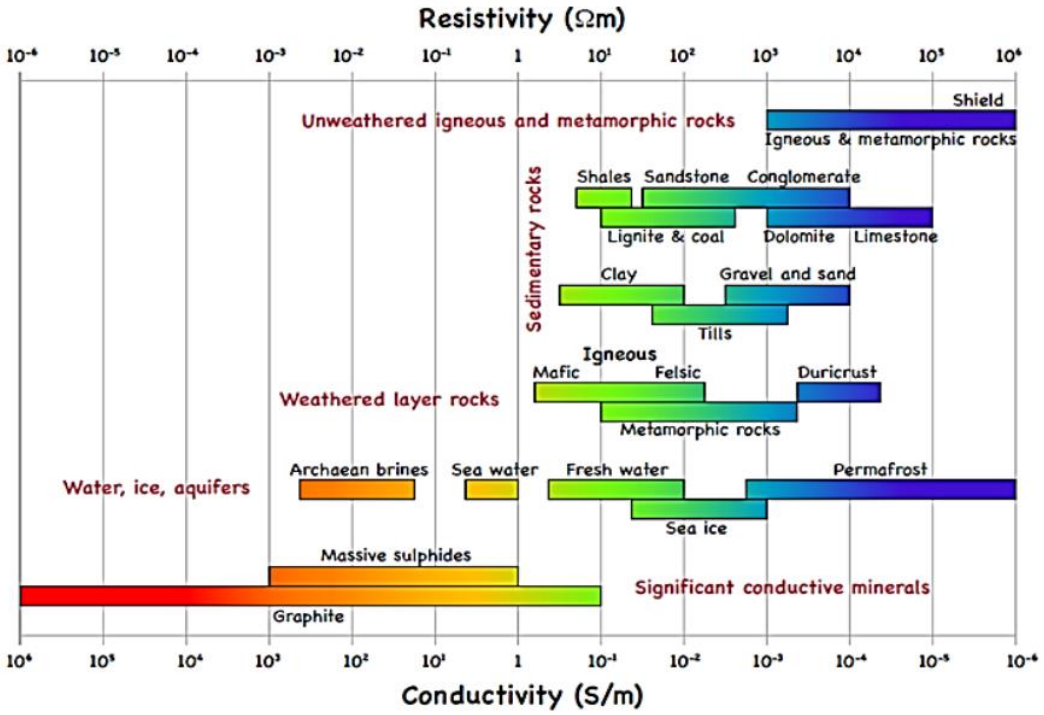


Figure 3. 8: Electrical conductivity and resistivity ranges of common earth materials retrieved from Palacky (1988)

CHAPTER 4: DATA ACQUISITION

4.1 Data acquisition, processing, modelling

4.1.1 Instrumentation

Electrical resistivity measurements were carried out using a system (fig 4.1) that comprises of a Syscal Pro Switch unit (Iris Instrument), 48 current and potential electrodes, 4 imaging cables, 48 connecting wires, 2 connecting boxes and a power source.

The Syscal Pro switch unit is an all-in-one multi-node resistivity and induced polarization imaging system used in environmental and engineering geophysical studies. It is a 10 channel receiver and transmitter which allows the acquisition of 10 measurements at a time. The system comprises of multichannel transmitters and receivers that enables a series of measurements to be taken (Iris Instruments, 2005). A multi-electrode system with N-channel(s) allows N number of data to be recorded concurrently and also by a factor of N increase the data acquisition speed (Aizebeokhai, 2010). It does automatic switching and can allow one to work with 48 electrodes (switch-48) or more.

The electrodes normally used are made of either bronze, copper, steel and aluminium and are connected to the imaging cable using insulated connecting wires of low resistance (Telford, 1990). The imaging cables are then connected to the back of the Syscal Pro Switch. Each imaging cable is 120m in length, depending on the total spread length required, i.e. for 480m, two cables are directly connected to the Syscal Pro Switch; connector boxes are then used to link or extend the cables; hence a total of four cables that totalled 48 electrodes are used (480m length).



Figure 4. 1: Field photographs showing acquisition equipment used, comprising (a) the Syscal Pro switch unit and a battery (b) connector box connecting imaging cables (c) steel electrode connected to the imaging cable by a connecting wire

4.1.2 Field Procedure

In this study, field resistivity data was obtained along fourteen traverse lines oriented Northeast-Southwest. The locations and orientation of the fourteen (14) profiles is shown in Fig. 2.3(b &c) Acquisition was carried out over a period of 24 days; of which 14days was used in line cutting to create a more open space to provide access along the profile for easy cable rollout during acquisition. The remaining 10 days were used for data acquisition. The first set of data acquisition consisting of 9 lines were acquired between May and August 2019. Data for the remaining 5 lines were acquired between January 2020 and February 2020.

To obtain the apparent electrical resistivity data along the profiles, a multi-electrode system was used. The system comprises of a switch-48 Syscal Pro resistivity meter connected to a total of four multi-cable systems each with 12 outputs. A linear arrangement of the system with a total of 48 electrodes with a maximum electrode spacing of 10m was set up.

Two types of parameters prior to electrical prospection were set using Electre Pro: geometric and acquisition parameters. The geometric parameters included; electrode number (48), electrode spacing (10m), which is constant. In this study, the maximum electrode separation of 10 m was used such that the maximum investigation depth of 97 m and 73m respectively for standard sequence and roll along sequence is achieved. Other geometric parameters include the electrode configuration. The dipole-dipole configuration was used due to its sensitivity to horizontal changes (Al-amoush et al., 2017) or its improved lateral resolution.

Acquisition parameters included the maximum standard deviation value allowed for the field data, this is the data quality factor and was set at 3%. The time cycle was set at 2s and the minimum and maximum number of stacks was set at 3 and 6 respectively. The parameters are set in order to improve the signal to noise ratio without affecting the rate of acquisition. The parameters were the same for acquisition of data along all the profiles for consistency.

The cables were rolled out along a survey line, stainless steel electrodes were then placed next to the cable nodes. To establish a good contact between the ground and the electrodes; the electrodes were driven at least half their length into the ground. Connecting wires were then used to connect the electrodes and the cable nodes.

Predefined measurements protocols and the contact resistances (ground coupling) are automatically checked by the Switch pro unit (Dahlin, 2001). Where high contact

resistances were encountered (e.g. systematic errors that result from insufficient current injection due to high electrode-ground contact resistance (Al-amoush et al., 2017)), they were successfully lowered by compacting the soil surrounding the electrode and also adding some brine. The Syscal pro switch then records direct readings of the injected current, potential difference, electrode position and apparent resistivities (Fazzito et al., 2009) as guided by the predefined parameters.

A differential Global Positioning System was then used to record coordinates and elevation reading along the survey line next to each electrode placed. Recording changes in the ground surface elevation is important as the values are incorporated in the inversion process of the data for accuracy. Topography is incorporated such that it becomes part of the mesh as part of the inversion.

When carrying out inversion using the Res2DInv program; incorporating topography into the inversion can be carried out using four different options available; the finite-difference method, and the other three using the finite-element method (Loke, 2000)

The finite difference method uses the Schwartz-Christoffel transformation, an approach that maps an undulating surface 2-D region into a rectangular mesh to calculate apparent resistivity values (Loke, 2000). The remaining three methods use a distorted mesh of the finite-element. The nodes on the surface are shifted or adjusted up and down to match the topography and their difference is on how the nodes are shifted (Loke, 1999).

Subsurface and surface nodes can be shifted by the same amount along the same vertical mesh line, this is applied in cases where topographic variation is not significant. Exponentially reducing or shifting the subsurface nodes does not affect the nodes at depth. This is a more applicable approach as the effect of the topography reduces with increasing depth. The last shift is determined by the Schwartz-Christoffel transformation method which calculates the amount of shift required (Loke, 1999).

4.1.3 Field Procedure- ROLL ALONG

The roll along technique is used if the survey line length is longer than the system length hence used to do an extension (Bernard et al., 2006). The extension is achieved by shifting a part of the layout along the survey line to make measurements in areas not already covered (Aizebeokhai, 2010). Figure 4.2(a) presents a layout of a typical roll along sequence. The procedure is that after acquiring the first set of readings with the standard sequence (a, b, c,

d), segment a is shifted and placed after segment d to form a new sequence combination (b, c, d, a) (Iris Instruments, 2005), figure 4.2(b).

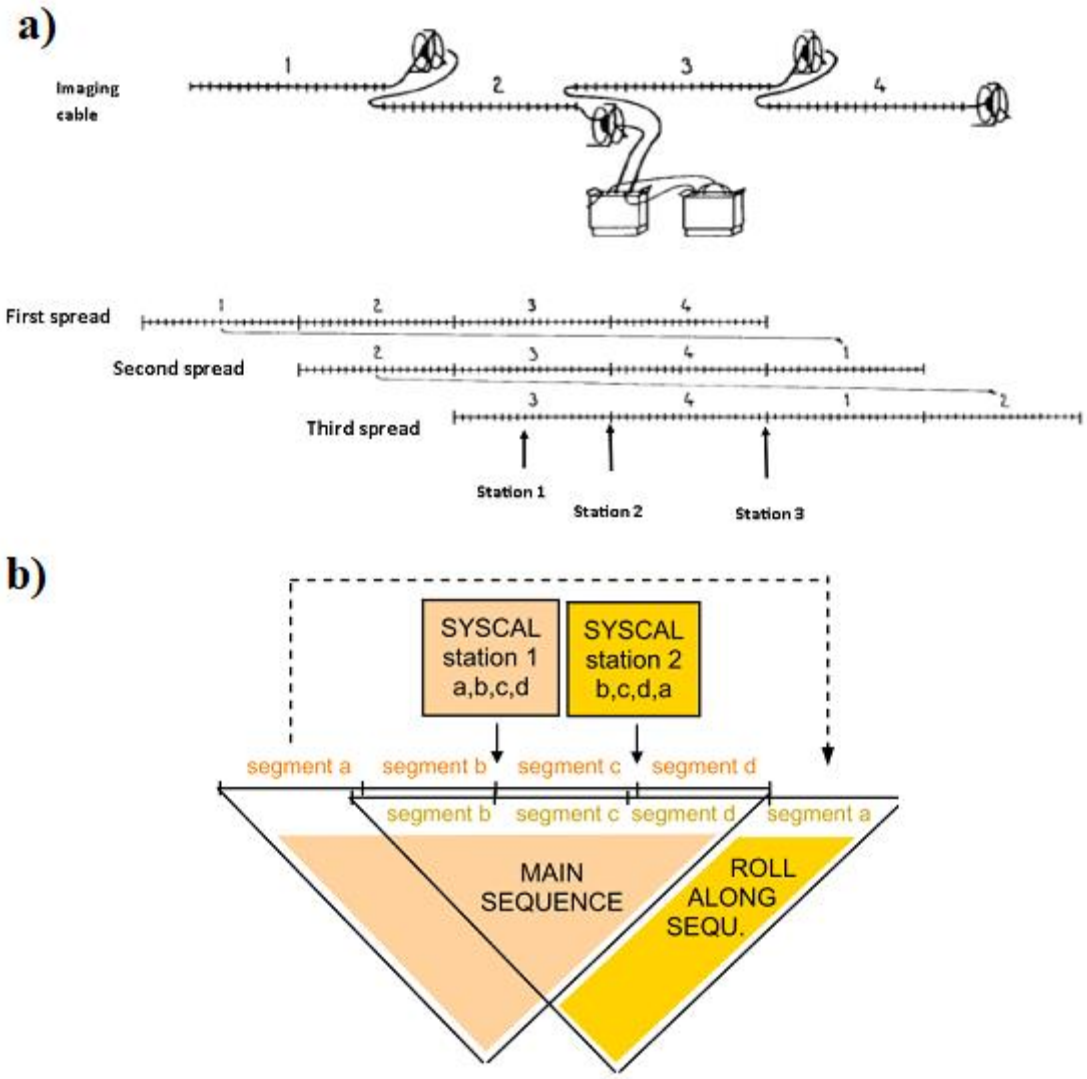


Figure 4. 2:(a) Schematic layout of the roll-along technique using four electrode cables (modified from Overmeeren and Ritsema (1988) as cited in Aizebeokhai (2010)), (b)Schematic diagram of the roll along method adopted from Iris Instruments (2005), segment a shifted after the standard sequence measurements to extend the system length,

In this study a roll-along technique involving a two-segment cable (a and b) was used to cover a survey line length of 720m, one segment comprised of two cables (with a total of 12 electrodes each). After the completion of the first set of measurement, the cable at the start of the system was moved and connected to the last cable (cable 1 connected to cable 4) to complete another set of readings. This process was carried out until the intended line length was covered.

The first set of readings acquired were for the standard sequence dataset; station 1 was used alongside segment a and b (fig 4.3). The maximum depth of investigation reached was 96m for the 480m spread. Reading 2 was acquired by extending the standard sequence by ¼ equal to 120m. Cable 1 in segment a was moved and connected to the end of segment b and data acquired using station 2. The distance covered was extended up to 600; the extension lead to a decrease in the depth of investigation by ¼. After acquisition of reading 2, cable at the start of the line was moved and connected at the end, covering a distance up to 720m, this extension also decreased the depth covered. The overall maximum depth of investigation reached which ensures a continuity of the bottom for this survey was approximately 73m, equal to ¾ of the initial depth reached (fig 4.3).

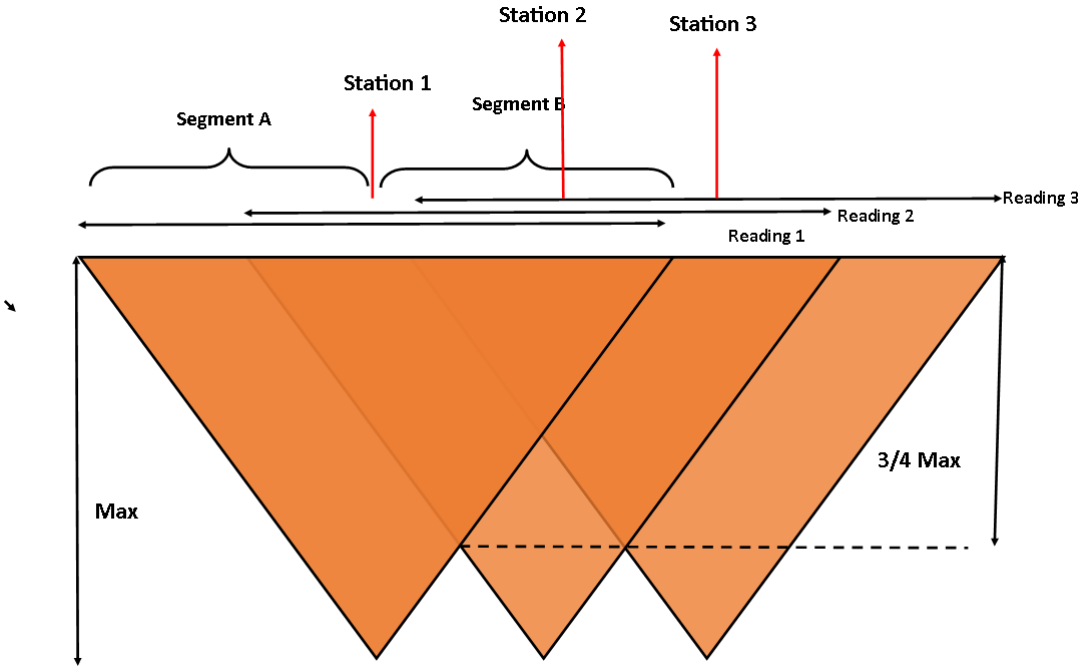


Figure 4. 3: Diagram showing the roll along technique as used in this survey showing measurements for the standard sequence (far left), followed by the roll along configuration. The maximum depth reached for the roll along configuration which ensured continuity in the bottom part is ¾ the maximum depth of the standard sequence.

4.2 Data handling

4.2.1 Data transfer and processing

Transferring and pre-processing of the recorded data by the Syscal pro switch was carried out using PROSYS II software; a program used in the transfer, editing, processing and exporting of resistivity and chargeability data acquired using the IRIS Instruments resistivity-meters and IP receivers (Iris Instruments, 2005).

The raw data from the Syscal pro switch unit, the (*.pro) file is read using the Prosys II software. Pre-processing involved filtering the data by removing all the Rho zero values as they in most instances mask other resistivity values when viewed from the Rho pseudosections. It is also used in applying absolute rho values and inserting topographic data acquired by a differential geographic positioning system. The Pre- processed data is then exported to various formats (″txt″, .dat).

4.2.2 Data error sources

Prior to carrying out inversion on the acquired data set, the general rule is to assess the pseudosection plot and the profile plot for bad data points. Such points affect the results as a good model is a function of good quality data. Bad data points are either systematic or random noise. Systematic noise is encountered when carrying out the survey where the obtained readings do not represent the true resistivity measurement. These points are caused by breaks in the cable, poor contact between the electrodes and the ground resulting in insufficient current injection, wrong connections of the cables and gaps caused by clips that are not attached to the electrode. Random noise includes effects of telluric currents that cause readings to either be higher or lower when compared to noise free readings (Loke, 2000; Zhou and Dahlin, 2003; Sjodahl, 2006)

4.2.3 Data quality control and assurance

In order to ensure data quality, filtering out bad data points was carried out using notepad++, extermination of the bad data points in the inversion software and root mean square (RMS) error adjustment. In notepad++ resistivity values were analysed, through the process off-range values (very low or high resistivity values) were manually deleted.

Bad data points with random noise are not that obvious. They are difficult to remove manually especially when dealing with a large data set. An error distribution bar chart (fig. 4.4(a)) from the Res2DINV program is used. The first inversion is carried out with all the data points and the results displayed for analysis. The 'RMS error statistics' option is then used to display the distribution of the percentage difference between the logarithms of the calculated and measured apparent resistivity values in the form of a bar chart (Loke, 2015). The highest bar (fig 4.4(a)) shows data sets with low errors and the bar height decreases with increasing error level. To remove the bad data points, the green cursor line is shifted to the left. Data points with higher errors remain in the right side of green cut-off line and are usually removed and the remaining points reinvented to get an improved model.

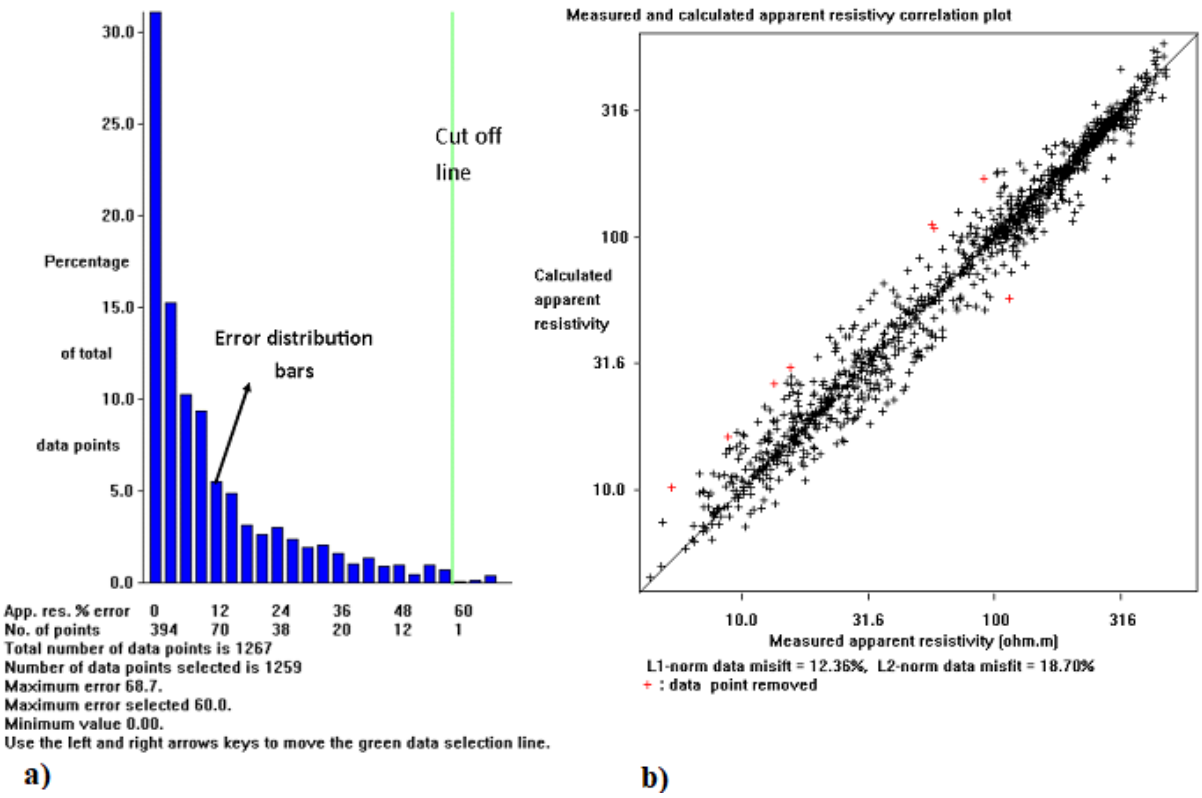


Figure 4. 4: RMS error modification using error distribution bar for line 9. (a) Error distribution bar showing the cut off line. Data points with higher errors are in the right side of green cut-off line (b) Error distribution points showing the modification done using the cut off line. Red points represent bad excluded points

Bad data points with systematic noise are removed using the "Extermination of bad data points" option in the Res2DINV program. In profile form they easily stand out as they show up as spots with usually high or low values from majority of the reading. The points are removed by selecting such points to exclude them during processing.

4.2.4 Data Interpretation

They are a wide range of resistivity variations in the subsurface with some materials exhibiting similar resistivity values. Similar resistivity values between different materials is a challenge during interpretation as they create a lot of uncertainty. It is recommended to do a detailed evaluation on the geology of the area under investigation to get a comprehensive understanding of the distribution of materials of the subsurface. Understanding also the factors affecting resistivity measurements is important in interpretation and such factors include;

The problem of non-uniqueness- it is a challenge in trying to determine a true, quantitative model of subsurface resistivity; this is because the same set of data can produce a wide range of models whose calculated apparent resistivity values are equally consistent with the measured values (Loke, 2000). A model with defined thickness with a certain resistivity value can portray the same inversion results as the model half its thickness having double its resistivity value (Telford & Sheriff, 1990).

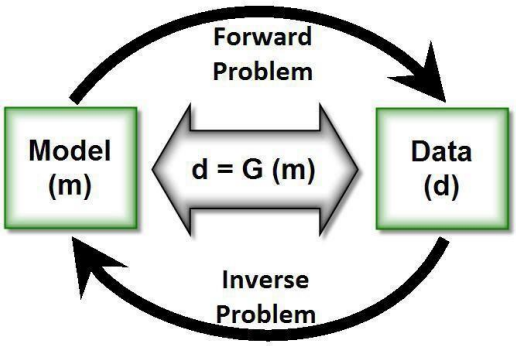
The resolution of the model is also determined by the data points. Points at the sides of the model are few and their effect is determined by the boundary conditions and the weight assigned to them (Nthaba, 2017). Extending the survey line to exceed the structure of interest can reduce their effects on the final model interpretation.

The resistance of the surface is also a challenge as it results in restricted current injection. Where the resistance is very high, the current injected into the ground is limited or equal to zero. If less current is injected, the resistance it encounters makes it difficult for it to penetrate deeper depths. Current penetrating through different materials alters its course through the materials accordingly. Alternatively, if the top most layer is of high conductivity, current is channeled through this layer and in most instances does not reach deeper depths structures (Sjodahl et al., 2008).

4.3 Data modelling

4.3.1 Inversion and forward modelling relationship

The measured data and the quantity of interest are linked using a mathematical relationship. Figure 4.5 is an illustration that links the data to a model, as well as forward modelling and inversion. Inversion process results in the generation of a generic model, whilst in forward modelling, synthetic dataset is modelled. Throughout the whole process the models are compared for equivalency, the forward model is altered until a better model similar to the inversion model is generated, a process known as iteration of the inversion.



Collected data (d) and the model (m) of a physical property are related by a mathematical function (G). Using a model to calculate a synthetic data set is known as solving a forward problem. Using a collected data set to generate a model is known as solving an inverse problem.

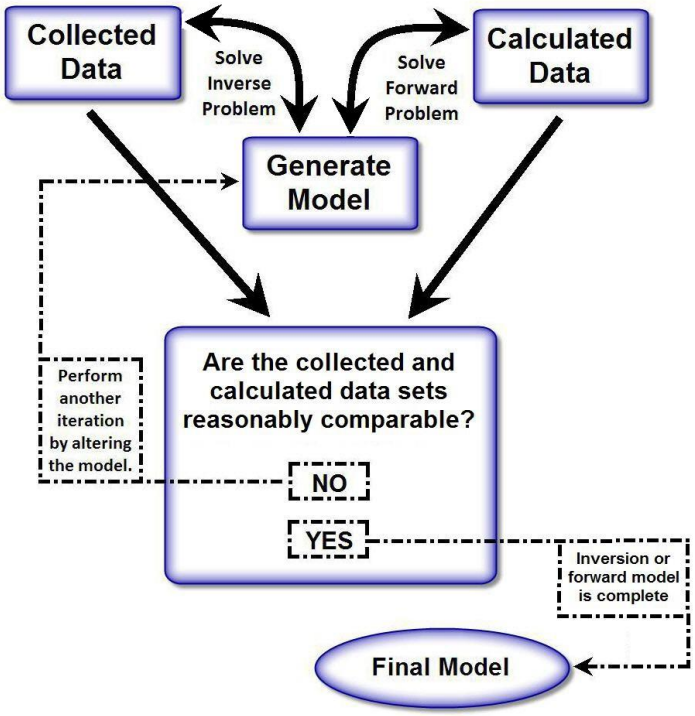


Figure 4. 5: Flow chart showing the relationship between data inversion and forward modelling adopted from Basin et al.(2012).

4.3.1.1 Inversion modelling

Inversion modelling involves applying mathematical problems in science to transform a set of observed data to reconstruct a subsurface model whose response agrees with the measured data. The inversion software used, Res2Dinv and Res3Dinv are computer programs that uses data obtained from electrical surveys to generate 2D/3D models for the subsurface (Griffiths and Barker, 1993). They are also cell based method (fig 4.6), the

parameters for the model are the resistivity values of the model blocks and the data is the measured apparent resistivity values (Loke, 2000)

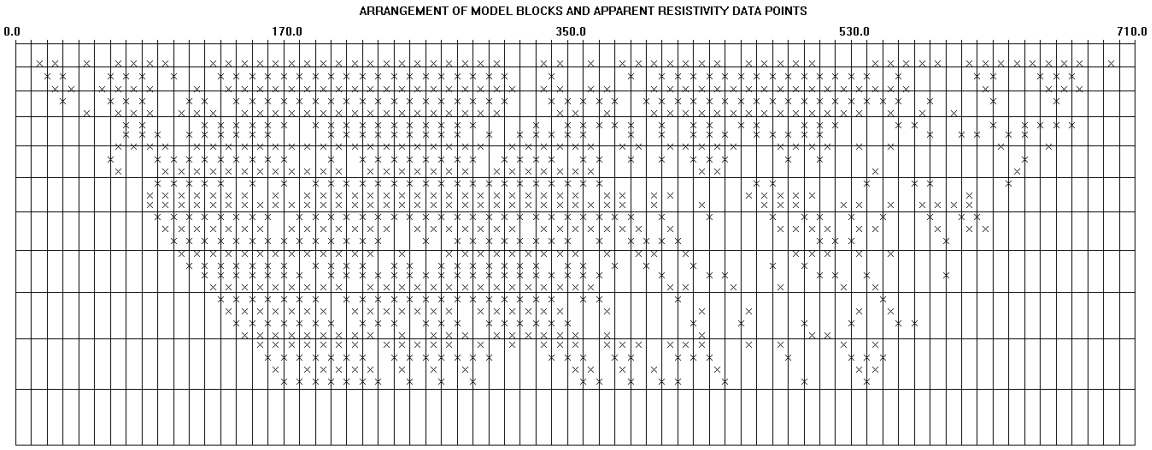


Figure 4. 6: Model blocks with data points plotted from line 4 plotted by Res2DINV, the x-axis represent the electrodes covering a distance of 720m, the y-axis represent the pseudodepth. The cross hair (x) represents the data points.

The blocks arrangement is generated automatically by the program. The distribution of the data points in the pseudosection depends on the optimization method used (Sjodahl, 2006). In order to determine the appropriate resistivity value for each block a least-squares inversion scheme is used (Loke, 1999).

The inverse modelling carried out during the processing of data enables the identification of anomalous regions during the interpretation of pseudosections. The blocks at the bottom row are set to approximately represent the depth of penetration resulting from the penetration from the largest electrode spacing (Edwards 1977).

The geology of the subsurface acts as a guide in determining the optimization method to use to carry out the inversion process; if the subsurface bodies of interest has gradational boundaries, the smoothness constant method (l2 norm) is used (Loke, 1999) and the blocky optimization method (l1 norm) is adopted where the subsurface bodies have sharp contacts ((Loke, 1999; Loke et al., 2003)

The inversion routine program uses an iterative process that tries to reduce the difference between the calculated and measured apparent resistivity values. The first model(s) is altered to generate a model with apparent resistivity values that are closer to the measured

values. The software uses the parameters the user selects and then iteratively tries to refine the model until the set convergence limit is reached (Monahan, 2013). A widely used iteration process uses the smoothness constraints equation that can be modified to give better result (Loke, 1999). The general standard smoothness constraints equation is as follows;

$$(\mathbf{J^T J}+u\mathbf{F})\ \mathbf{d} = \mathbf{J^T g} - u\mathbf{F r} \quad (4.1)$$

Where **F** is the smoothing matric, **J**; the Jacobian matrix of partial derivatives, **r**; a vector of the logarithm of the model resistivity values, **u**; the damping factor, **d**; model perturbation vector and **g** represent the discrepancy factor.

Discrepancy vector, g, is given as a root mean square value. Model perturbation vector, d gives changes in the resistivity values in trying to achieve an improved model. The control on the weight on the smoothness in the inversion process is given as the damping factor, u (Loke, 2000).

4.3.1.2 Forward modelling

In forward modelling, synthetic apparent electrical resistivity values are generated to create a theoretical electrical resistivity model for the subsurface. The subsurface resistivity distribution of the type of structure intended to be surveyed is defined with the purpose to calculate the possible apparent resistivity for that structure. This synthetic model is then run using the Res2Dmod program (a 2-D forward modelling program)(Loke, 1999).

The forward modelling subroutine forms an important part of any inversion program. It is important to calculate the theoretical apparent resistivity values for the model produced by the inversion routine, it is used as a reference for measuring its level of agreement with the measured values (Loke, 2000). In engineering and environmental surveys, it is recommended to use the finite-element and finite-difference methods as they are best suited for the subsurface with arbitrary resistivity distribution (Loke, 2000).

The finite-element method applies the standard first-order triangular elements (Silvester and Ferrari 1990) whilst in the finite difference method, the subsurface is divided into a rectangular grid which then decides the electrical potential for the nodes (Mojica et al., 2017). It determines the potential at the nodes for the rectangular mesh (Nthaba, 2017).

Forward modelling is used to aide in survey planning and results interpretation. In survey planning it is used to help in the selection of an array suitable for a particular survey. Some of the factors considered include the cost estimates, intended depth of investigation, array resolution and practicality of the intended survey. Different arrays have different responses to the same structures and their resolution is depth affected (refer to table 3.1). Prior to field survey, certain information about the target of interest such as its shape and size is normally known. Forward modelling is used to test different arrays to find a better suitable array that can effectively map the structure of interest. The modelling is also used to determine the suitable spacing between adjacent electrodes and also the maximum spacing that can be applied. Forward modelling is also used to validate or nullify the interpretations made based on the measured data (Nthaba, 2017) as is the intent for this research.

4.4 Data analysis

4.4.1 Forward modelling

Due to the absence of boreholes within the area of study to substantiate the results of the geophysical survey against the stratigraphy of the area, a forward model was generated. The forward model is used to align the field resistivity data roughly with a potential representation of the subsurface resistivity (Kress et al., 2004).

After analysing the field data, forward modelling was then used to calculate apparent resistivity values from a user defined two-dimension grid of rectangular model blocks. The model blocks are clustered into layers corresponding to the layers found in the inverted field resistivity data (Kress et al., 2004). The constructed forward model is used in the computation of apparent resistivity values. Processing of the apparent resistivity values was done following the same procedure used in the processing the field resistivity data using the Res2DINV software.

Changes to the forward model were made using the iterative method to improve the correlation with the inverted field model (Ball et al., 2004). The resulting model from the synthetic inverted data is then compared to the model from the inverted field resistivity data (fig. 4.9). A forward model resolution is achieved when the inverted field resistivity data and the synthetic inverted model datasets roughly correspond. The grid from the final forward model is used to provide a comprehensive subsurface interpretation (Degnan et al., 2001).

A layout of 72 electrodes was modelled using a dipole-dipole array with the electrode spacing set at 10 m. Synthetic apparent electrical resistivity values were then calculated using the Res2Dmod forward modelling program. The subsurface model created comprised of different layers with different resistivity values (Fig. 4.7). The assigned resistivity values on each layer were based on the field resistivity data. The shallow depths comprise of a low resistivity layer of about 1 Ωm resistivity with an interbedded layer of resistivity about 100 Ωm. The two resistivities are a representative of mudstone and sandstone respectively. Another low resistive layer was modelled representative of siltstone with resistivity value of about 10 Ωm. The other layers were assigned high resistivity values of 1000 Ωm and 3000 Ωm respectively, a representation of coals with different resistivity values as per the rank. Coal rank (quality) is a result of the temperature and pressure from the burial depth. Deep seated coals are highly resistive due to less water content as a result of compaction (Suggate, 1974).

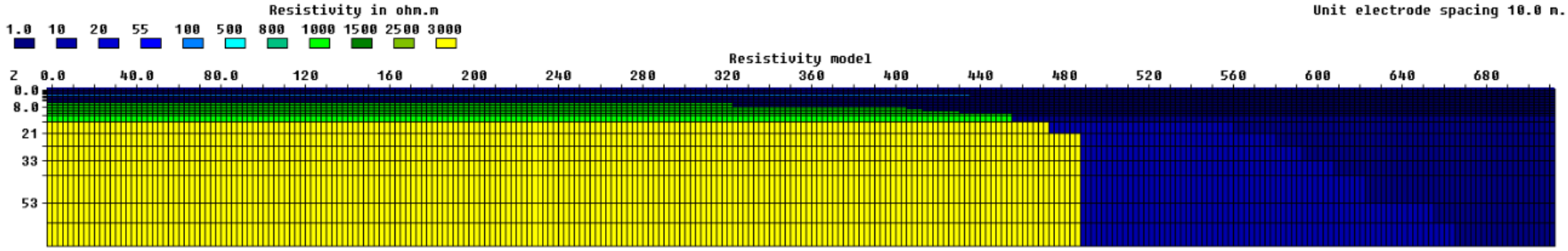


Figure 4. 7: Forward model simulating a fault structure in the study area. This model is made up of layers of varying thicknesses and resistivities. The shallow depths comprise of a low resistivity layer with an interbedded medium low resistivity layer. Underlying the low resistivity layer are the high resistivity layers representing coals of different resistivity values. The different resistivity shows a disturbed lateral continuity of the coal seams due to the inferred fault structure.

With every layer assigned a specific value, model modification was done by changing the thickness and depth of each layer. Following each modification and computation, an inversion was carried out on the model, the resulting model was compared with the inverted field data for

equivalency. After a general size and shape of the layers was developed, an anomaly representative of the fault structure was then introduced to the forward model.

The model with the anomaly is modified after each inversion until the inverted model anomaly resembles an anomaly corresponding to the inverted field resistivity dataset. The two models were then compared to the known geologic information, in this case the stratigraphic borehole log B55 (fig 2.4b) from Green (1961).

Finite-element computational method was used to compute the apparent resistivity values to construct the model (fig 4.8). The model has a total depth of 74 m; the inversion was carried out on a data set with 1635 apparent resistivity measurements. Before the inversion, Gaussian noise of 3% was added to the synthetic data set to incorporate disparities as field data always have the effects of noise (Robert et al., 2012). The synthetic data set was then inverted to give the measured apparent resistivity pseudosection (Fig. 4.8a), the calculated apparent resistivity pseudosection (Fig. 4.8b) and the inverse model resistivity section (Fig. 4.8c)

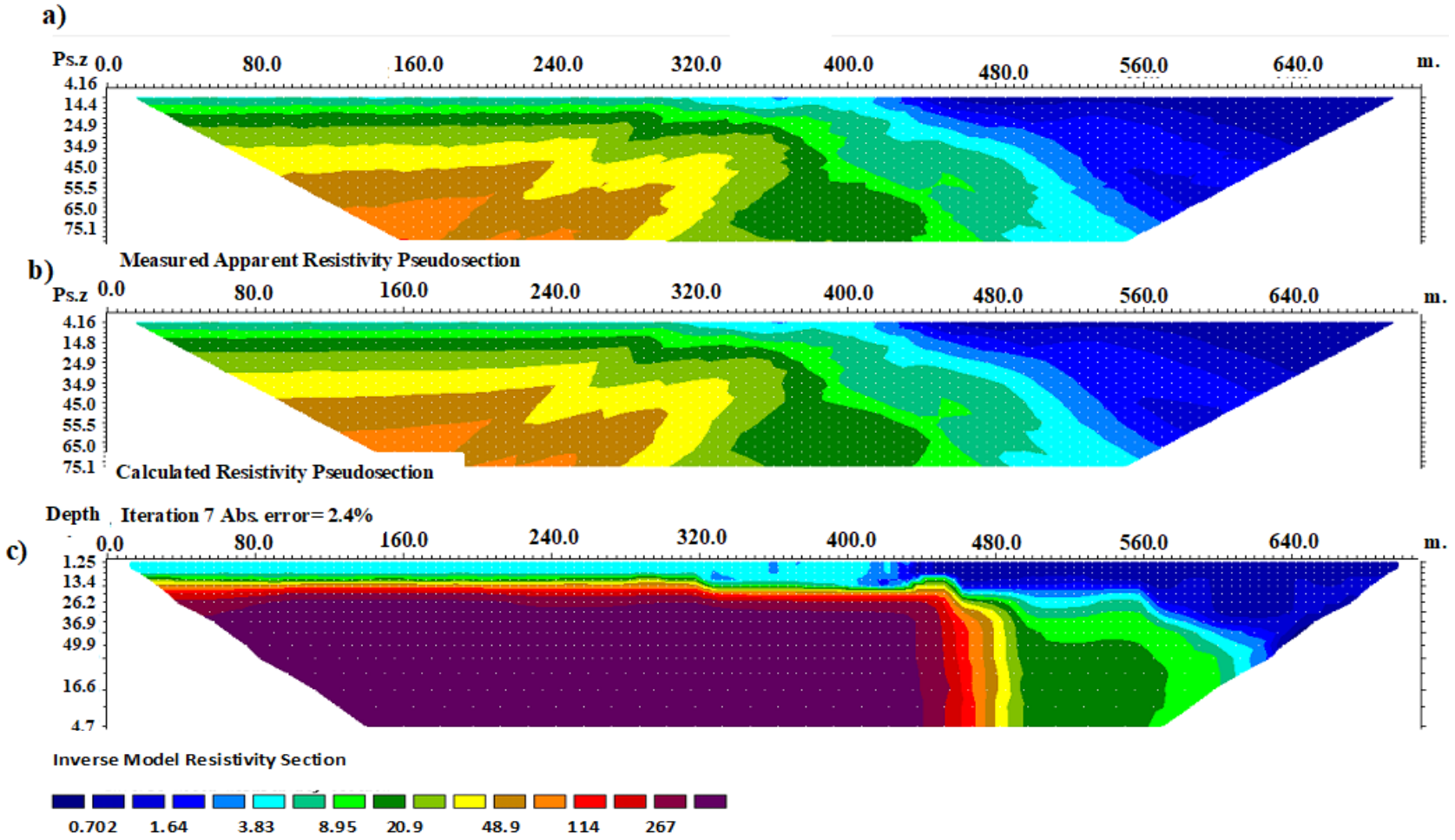


Figure 4. 8: Image of the results obtained after the inversion of the forward model (fig. 4.8), an idealized subsurface condition simulating a fault structure, (a) the measured apparent resistivity pseudosection, (b) the calculated apparent resistivity pseudosection, and (c) the inverse model resistivity section

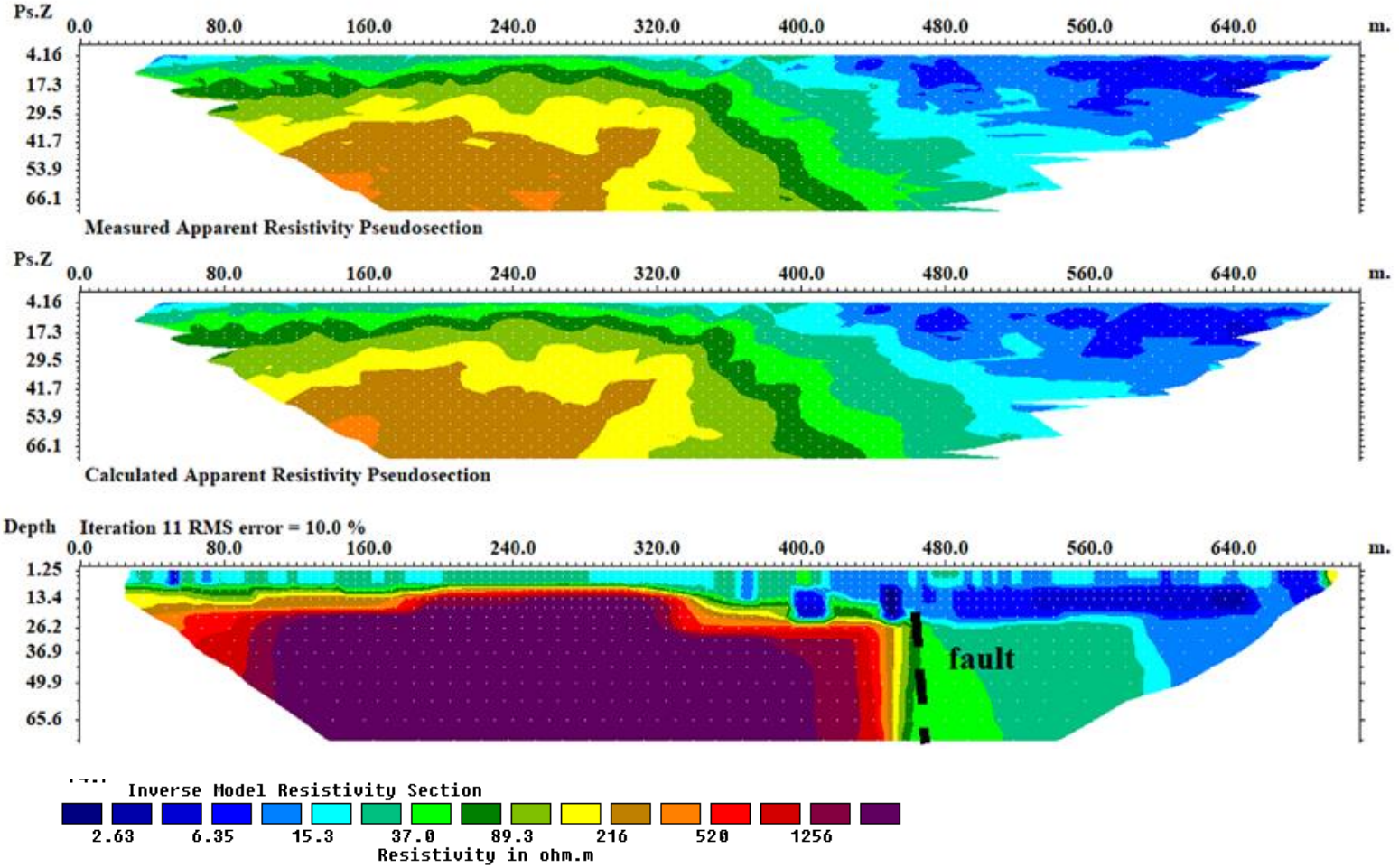


Figure 4. 9: The subsurface resistivity inversion results of the field data for a profile situated at y=450 m showing, (a) the measured apparent resistivity pseudosection, (b) the calculated apparent resistivity pseudosection, and (c) the inverse model resistivity section with an absolute error of 10.0 %. The y-axis show elevation/depth and the x-axis give the distance along the profile, all in meters

CHAPTER 5: RESULTS AND INTERPRETATION

5.1 Results introduction

Fourteen 2D electrical resistivity tomography lines "Profile 1 to 14" were collected using the Syscal Pro switch system. The ERT profiles trend northeast to southwest, roughly perpendicular to the investigated fault trace. For localization and determination of elevation along the profiles a Differential Global Positioning System (DGPS) was used. The generated 2D inverse resistivity sections were correlated with the stratigraphic borehole log B55 (Green, 1961) and the interpretation of the lithology of Mmamabula area by Green (1973).

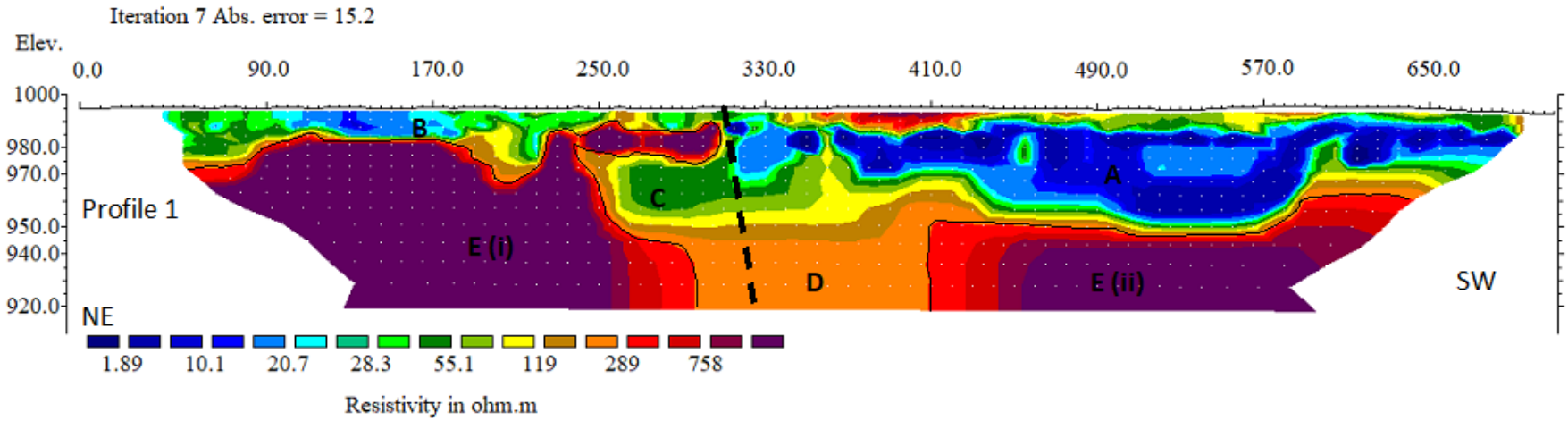
The inverse resistivity sections were interpreted to investigate structures in the study area so as to understand their relationship with subsurface placement of the coal seams. The plot of the pseudosections show the subsurface imaging depth restricted at approximately 73m. The results show an electrical resistivity range from approximately 1.89 to 758 Ωm. Borehole log B55 (fig 2.4b) was used as a reference to attribute the different resistivity values to the different lithologies. Each resistivity anomaly range (A to E; Figure 5.1) observed represent a lithological unit. The observed differences between zones with the same anomalies is an indication that there is spatial geometry variability in the Mmamabula (Williamson, 1996).

The resistivity range showing low resistivity anomaly values of about 1.89 to 10.1 Ωm (dark blue/light blue) were assigned anomaly A, representative of mudstone/ shale inferred from borehole stratigraphic log B55 (Fig 2.4b). Resistivity values from 10.1 to 20.7 Ωm (light blue/blue-green) were assigned anomaly B, attributable to the sandstone & grit; anomaly C (light green/dark green) represents grey siltstone with a resistivity range from 28.3 to 55.1 Ωm. Yellow/brown/orange colors with a range from 119 to 289 Ωm are assigned anomaly D to represent mudstone with thin coal. Anomaly E represent high resistivity variations values from 289 to >758 Ωm (red/ purple) corresponding to coal as inferred also from B55 stratigraphic borehole log.

The above classification is also supported by Green (1973), he stated that the middle Ecca comprises of felspathic sandstone, grits, conglomerates and 2 coal zones; the 'lower coal', a semi bright banded coal with an average thickness of 2.4m, and the 'upper coal'- dull massive

type that has an average thickness of 15.5m (Green, 1975). The upper Ecca lithology comprise of blackshale and mudstone with numerous coals(Green 1973). A thin seam in some boreholes recorded by Green (1975), is found within the upper part of the mudstone overlying the upper coal and is termed the 'Thin upper coal'.

5.2 Two Dimension Resistivity models



Interpretation

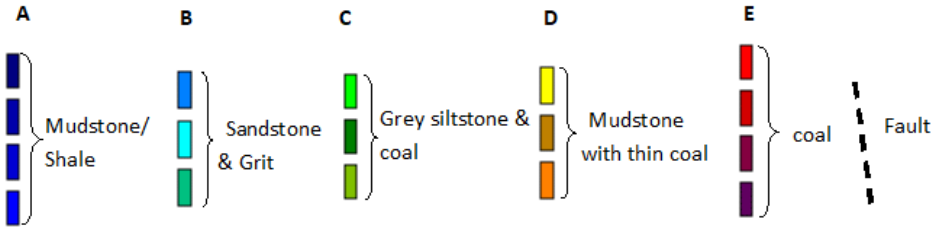
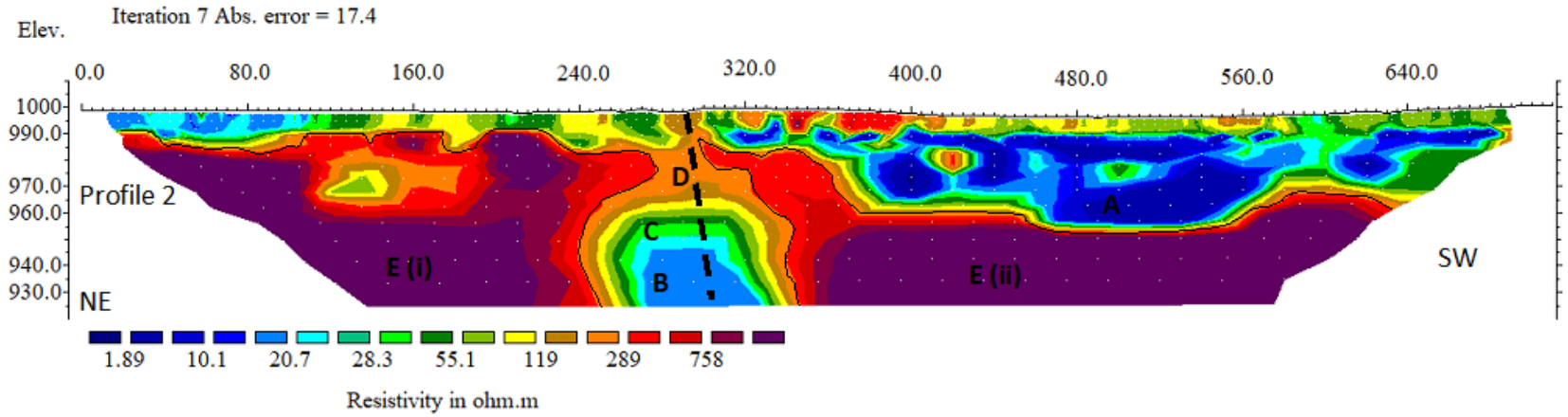


Figure 5. 1: Resistivity section along line 1 situated at y=0 m.

Profile 1 as seen in fig. 5.1 show the presence of grey siltstone , sandstone, mudstone and coaly material indicated in the section as anomalies B,C.D and E at depths near the surface. Anomaly A (mudstone/shales) occupies the SW portion of the profile and lies from aproxiamately 10m depth with a maximum thickness of 35m. Anomaly B (sandstone/grit) is not prominent in profile 1, anomaly C (grey silstone & coal) form as thin laminations around anomaly A. Anomaly D occurs mostly as thin laminations around Anomaly E and also as a thick layer betweem the E anomalies. Anomaly E is the most prominent layer, it occurs as a massive thick generally flat lying layer extending from depth 11m (E(i)) and 45m (E(ii)) to the base of the profile. This shows a displacement of approximately 34m vertically.



Interpretation

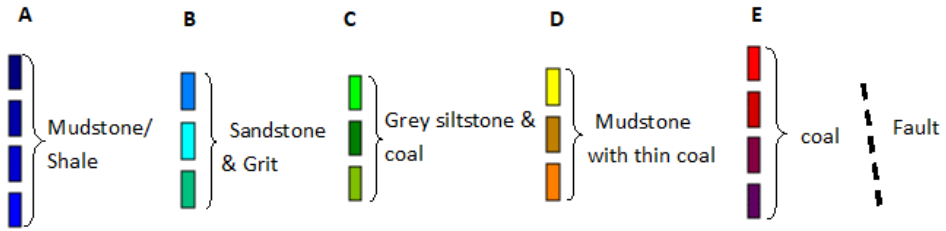
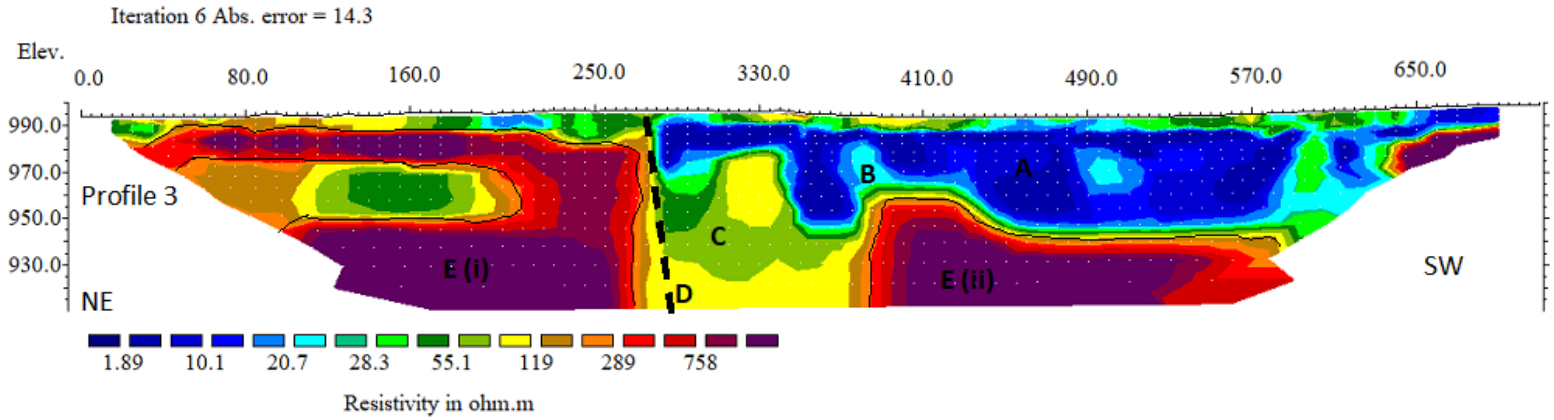


Figure 5. 2: Resistivity section along line 2 situated at y=50 m.

Profile 2 is dominated by high resistivity values. The most prominent anomaly is E; Anomaly E(i) is found at shallow depth, from 8 m below the surface and extends to the base, E(ii) is found from 37m depth and also extends to the base of the profile. The two high resistivity anomalies show a vertical displacement of approximately 29m. They is a lateral discontinuity between the coal seams, the SW shows the coals at deeper depth. The shallow depth across the profile length as seen in fig. 5.2 show nomalies B, C, D, E which are a representation of grey siltstone, sandstone, mudstone and coaly material. Anomaly A occupies the SW portion of the profile from aproxiamately 6m depth with a maximum thickness of 37m. Anomaly B forms as thin laminations around anomaly A and also forms as a protruding anomaly between anomaly E(i) and E(ii). Anomaly C forms as an embedded layer between anomaly B and D. Anomaly D also forms as thin lamination around anomaly E.



Interpretation

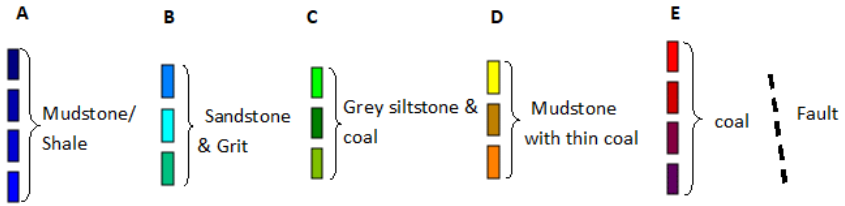
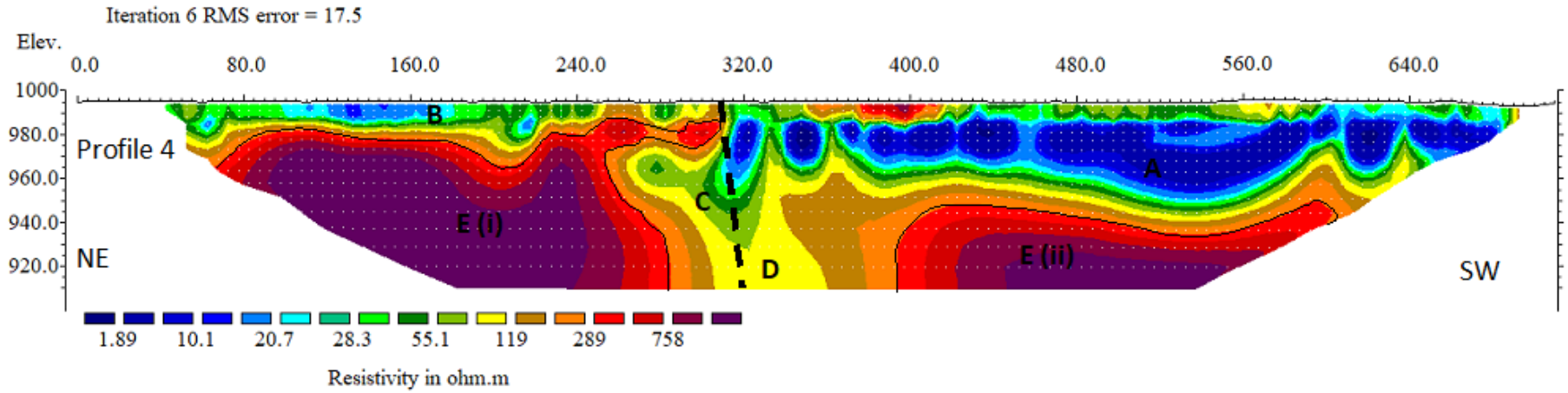


Figure 5. 3: Resistivity section along line 3 situated at y=100 m.

Profile 3 shows anomaly E representative for coal, found at both sides of the fault anomaly, E(i) in the NE side is divided into two layers; a thin upper layer from appoximately 5m depth with a thickness of 15m and another bottom laying layer from depth 45m extending to the base of the profile. Anomaly E (ii) which is in the SW portion of the profile is from a depth of 40m to the base of the profile. The two seams shows a displacement of about 35m vertically. They is also a contact observed as the NE side of the profile is dominated by high resistive layers compared to the SW portion.

Anomalies B,C and D which are a representation of grey siltstone, sandstone, and mudstone with coaly material are found at shallow depth. Anomaly A also occupies the SW portion from approximately 5m depth with a maximum thickness of approximately 47m thickness. Anomaly B appears as thin lamination around anomaly A. Anomly C is found in the centre of the profile and also embedded between anomaly D. Anomaly D forms as thin laminations around anomaly E.

Fig.5.4 show anomalies B,C, D, E which are a representation of grey siltstone and sandstone, mudstone and coaly material at shallow depths. Anomaly A occupies the SW portion from 10m depth with a maximum thickness 36m and is bounded by thin laminations of anomaly B. Anomaly C appears as thin laminations enclosing anomaly A and B. The most prominent anomaly-E, shows a displacemnt of approximately 35m vertically. In reference; E (i) is found from depth 11m whilst E (ii) is found at deeper depth of about 46m. Anomaly D is dominant in the centre of the profile and spreads out as as thin laminations around anomaly E.



Interpretation

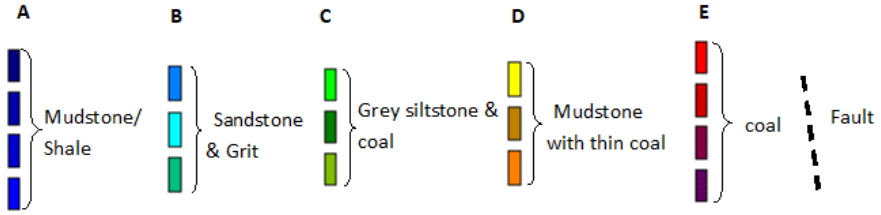
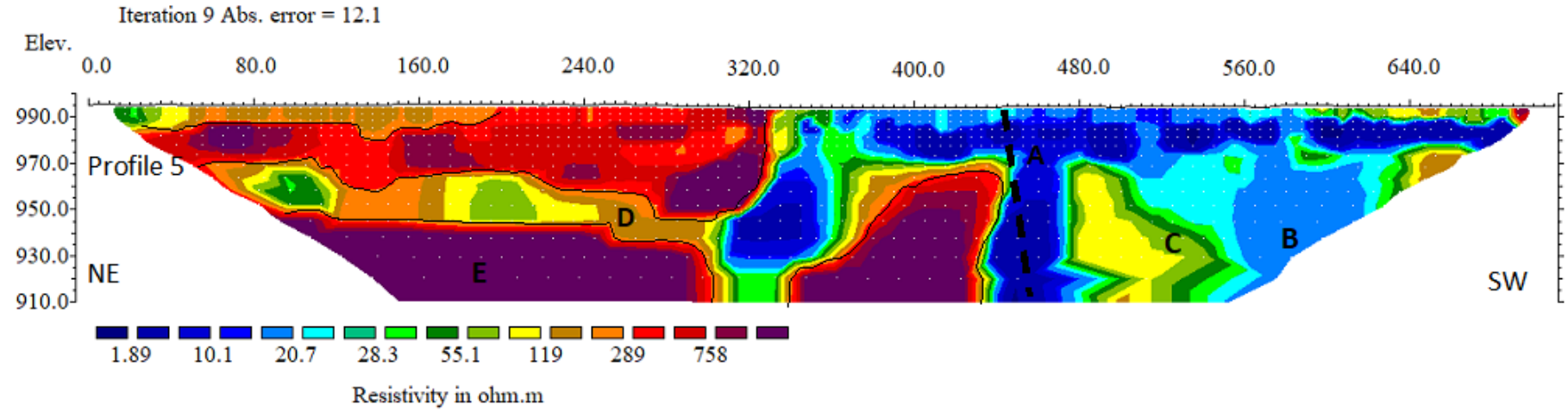


Figure 5. 4: Resistivity section along line 4 situated at y=150 m.



Interpretation

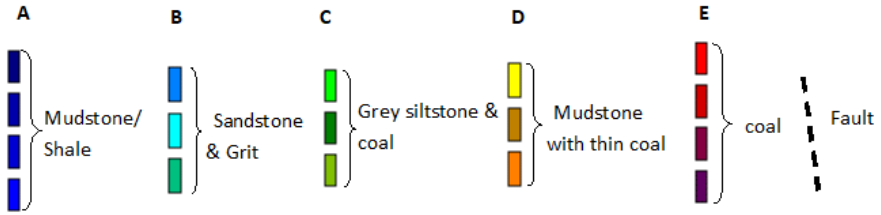
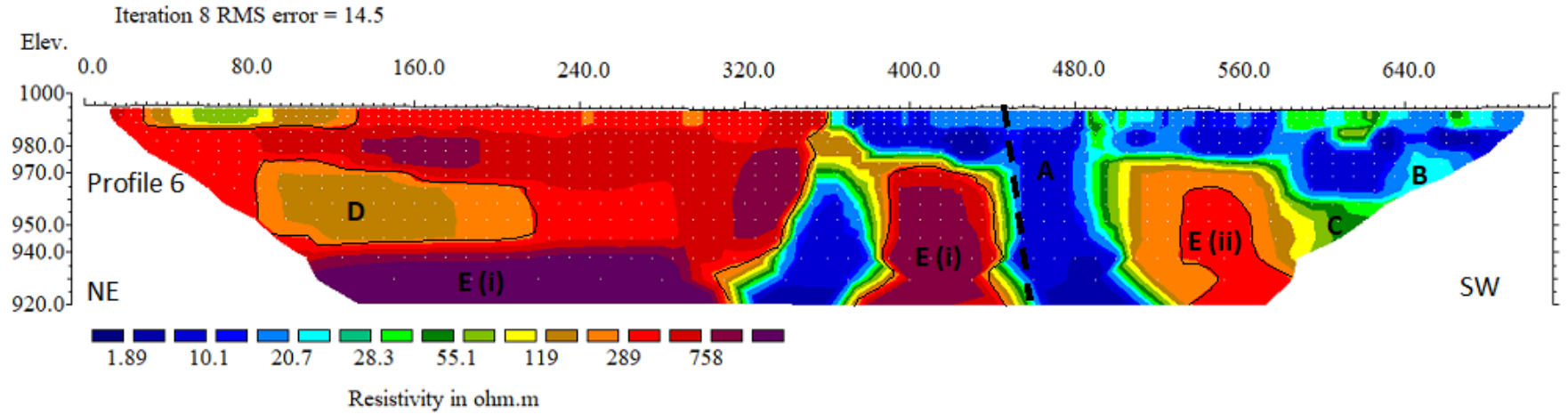


Figure 5. 5: Resistivity section along line 5 situated at y=250 m.

The shallow portions of profile 5 are dominated by anomaly A and E. Anomaly A which is a representation of shale or mudstone is restricted to the SW portion of the profile while anomaly E, a representation of coal is dominant on the NE portion. Anomaly B appear as laminations around anomaly A, whilst anomaly C appears as thin laminations around anomaly E. Anomaly D appears as an interbedded layer between the E anomalies.



Interpretation

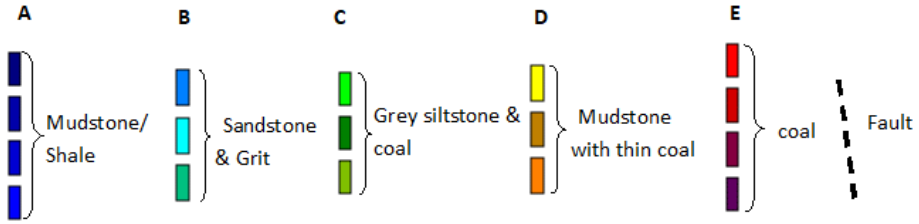
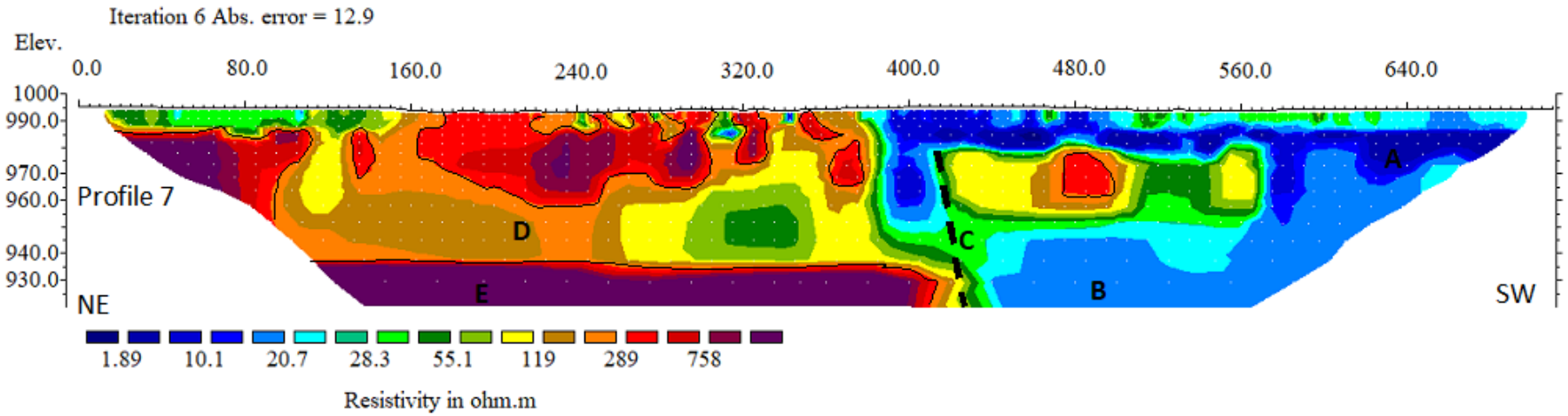


Figure 5. 6: Resistivity section along line 6 situated at y=300 m.

Profile 6 is dominated by anomaly A and E. Anomaly A which is a representation of shale or mudstone is restricted to the SW portion of the profile while anomaly E, a representation of coal is dominant on the NE portion. The fault anomaly is as presented showing the NE side of the fault dominated by high resistivity values whist the SW side is dominated by low resistivity values. Anomaly B forms as thin laminations around anomaly A.



Interpretation

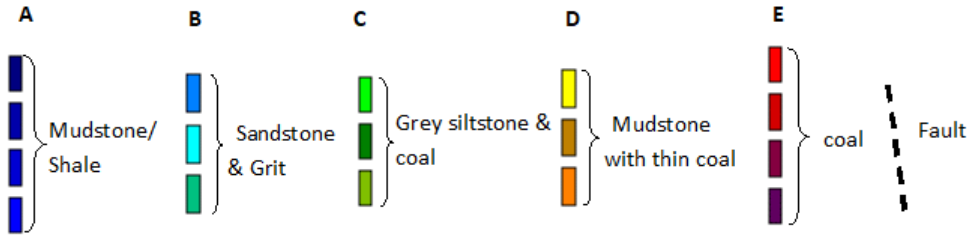
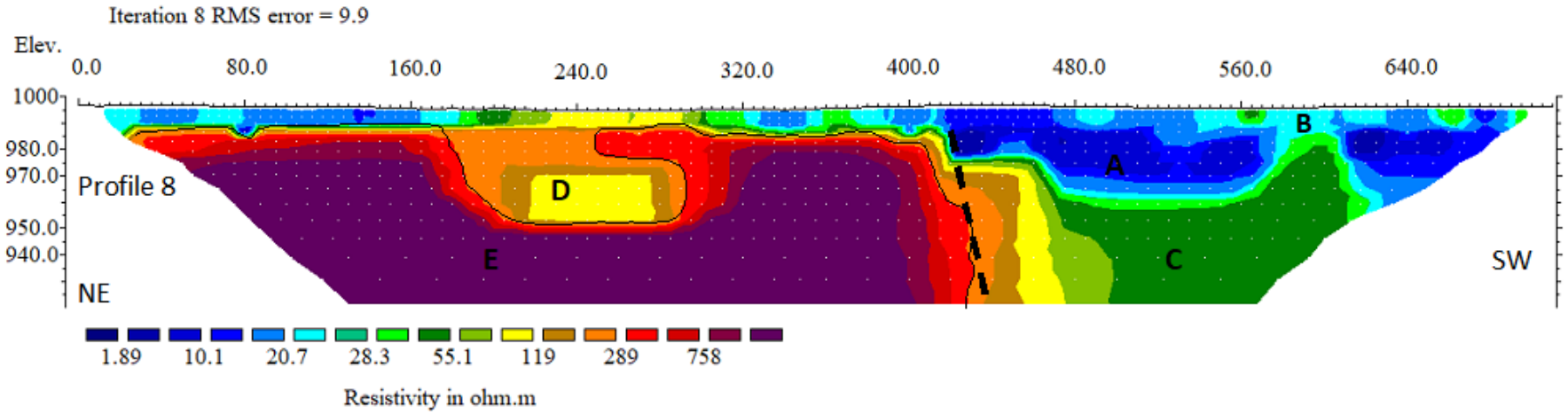


Figure 5. 7: Resistivity section along line 7 situated at y=350 m.

Profile 7 shows anomaly A potrayed as a thin layer occupying the shallowest SW portion. Anomaly B appears as thin laminations around anomaly A and also as a thick layer from 45m depth to the base of the profile restricted to the SW side. The NE portion of the profile is dominated by anomaly E which is divided into 2 layers. The shallow fragmented E anomaly is from 6m depth. The lower laying E anomaly is from depth 45m extending to the base of the profile. Another E anomaly appears as a fragment enclosed by anomaly D in the SW portion of the profile at 480 m distance

horizontally. Anomaly D forms as an interbedded layer between the E anomalies in the NE portion of the profile. The NE side of the fault anomaly is dominated by high resistivity values whilst the SW side is dominated by low resistivity values.



Interpretation

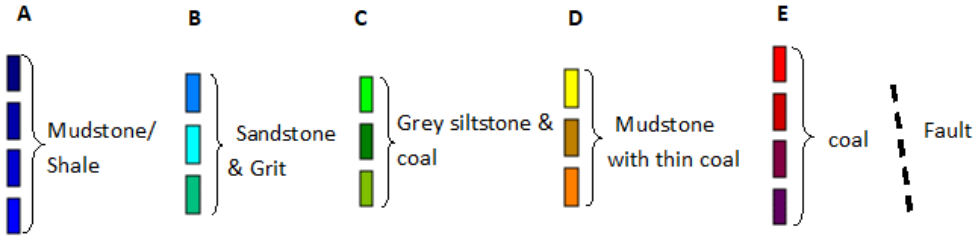
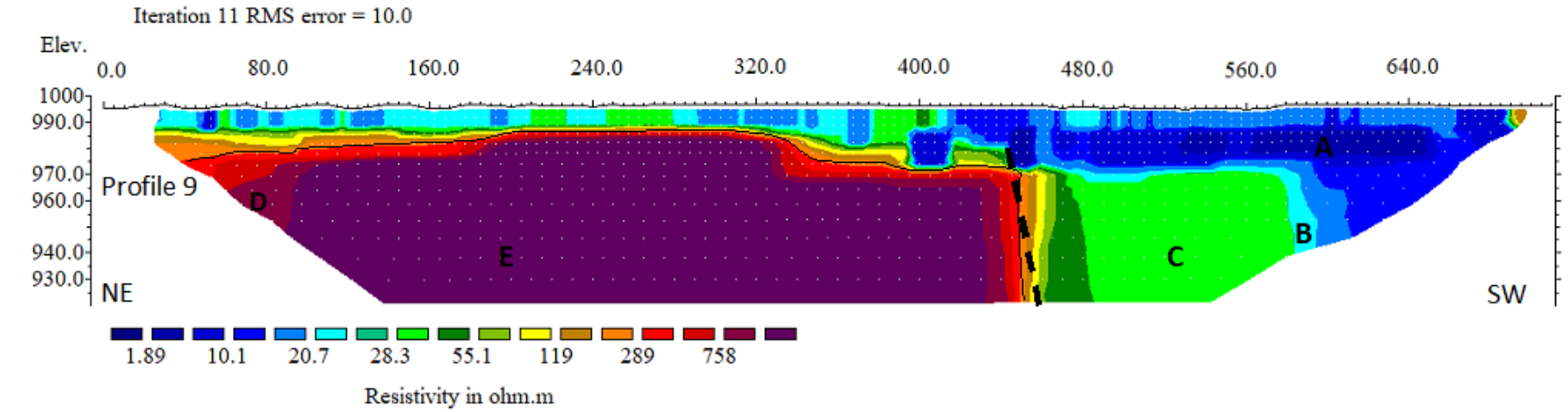


Figure 5. 8: Resistivity section along line 8 situated at. y=400 m.

The most prominent Anomaly for profile 8 is E (coal), it appears as a thick layer restricted to the NE portion of the profile. It extends from a depth of approximately 9m to the base of the profile. Anomaly D appears a lamination around anomaly E. The observed fault anomaly is as presented. It does not cut across anomaly A.

Principle of cross-cutting relationships states that younger features cut across older features hence since the fault does not cut across anomaly A, it can be concluded that anomaly A (mudstone/shale) deposition occurred later after the faulting had occurred. The NE side of the fault is dominated by high resistivity values, whilst the SW side is dominated by low resistivity values. At shallow depth, profile 8 is dominated by anomaly A, it forms a thin layer from the NE portion and thickens towards the SW portion. Anomaly B presents only as a lamination restricted around anomaly A. Anomaly C forms as a thick layer underlying anomaly A at depth 21m to the base of the profile in the SW portion of the profile.



Interpretation

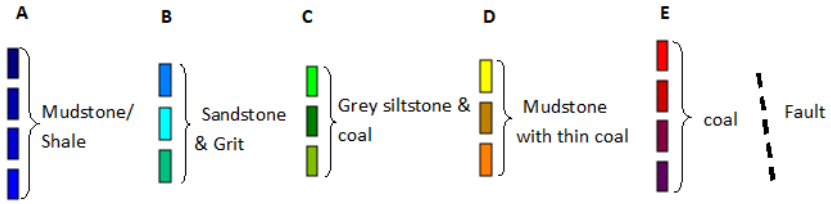
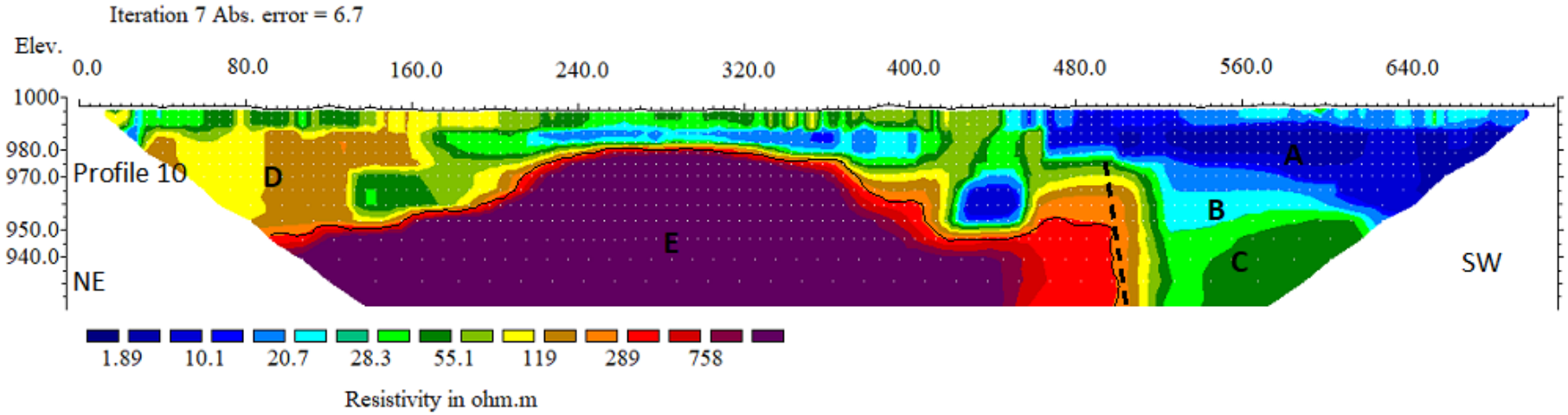


Figure 5. 9: Resistivity section along line 9 situated at y=450 m.

Profile 9 shallow depth is dominated by anomaly A and B forming a thin layer (minimum thickness 7m) that thickens towards the SW portion. Anomaly A dominates anomaly B as anomaly B appear as a lamination underlying anomaly A. Anomaly E appears as a thick layer that dominates the NE portion of the profile, it extends from a depth of approximately 9m to the base of the profile. Anomaly D appears as a thin lamination that overlies anomaly E. The fault also does not cut across anomaly A and B hence it can be concluded that anomaly A and B deposition occurred later

after faulting had occurred. Anomaly C forms as a thick layer that underlies anomaly A and B in the SW portion of the profile. The NE side of the fault is dominated by high resistivity values whilst the SW portion is dominated by low resistivity values.



Interpretation

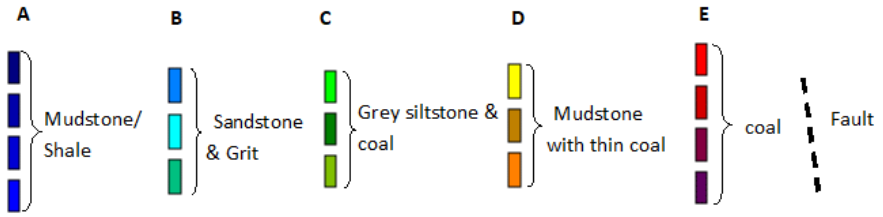
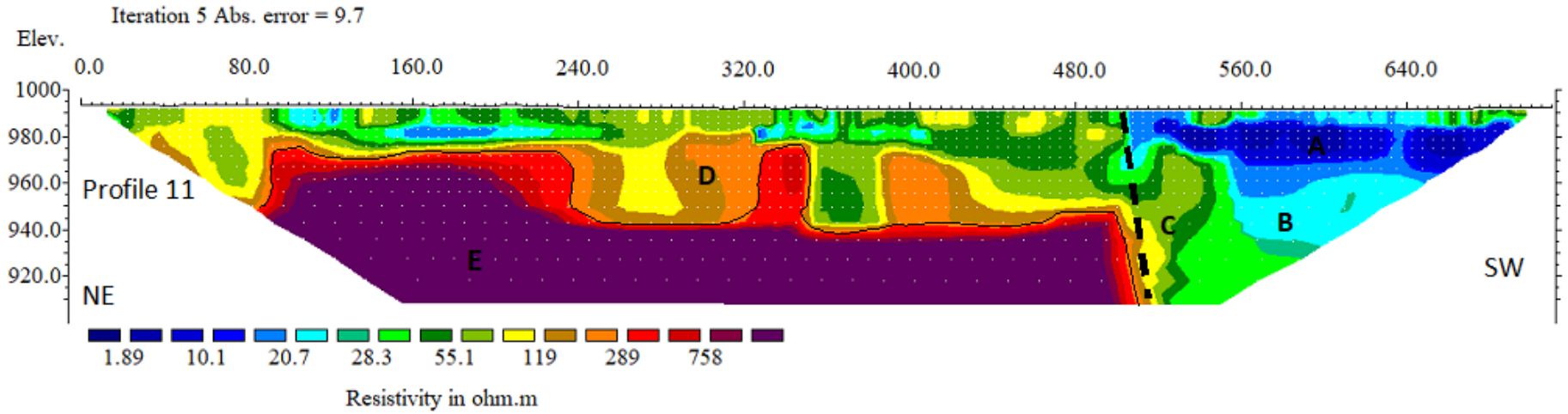


Figure 5. 10: Resistivity section along line 10 situated at y=500 m.

Anomaly C, representative of grey siltstone and coaly material dominate the shallow depths of profile 11, with a portion on the SW side showing Anomaly A, mudstone. The most noticeable anomaly is a thick 'dome shaped' coal layer (anomaly E) that extends from approximately 15m to the base of the profile. It is laminated by a thin layer of anomaly C. The fault anomaly is as presented, there is a clear transition, the NE side of the fault

anomaly dominated by high resistivity values ρ>119 Ωm whilst the SW side is dominated by only lower resistivity values ρ<119 Ωm. The fault does not cut across anomaly A, it can be concluded that anomaly A (mudstone/shale) deposition occurred later after the faulting had occurred.



Interpretation

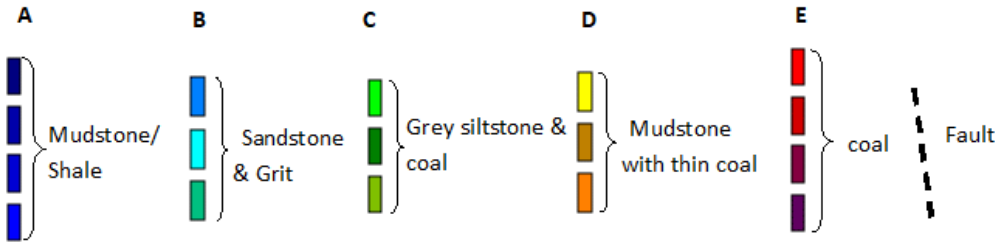
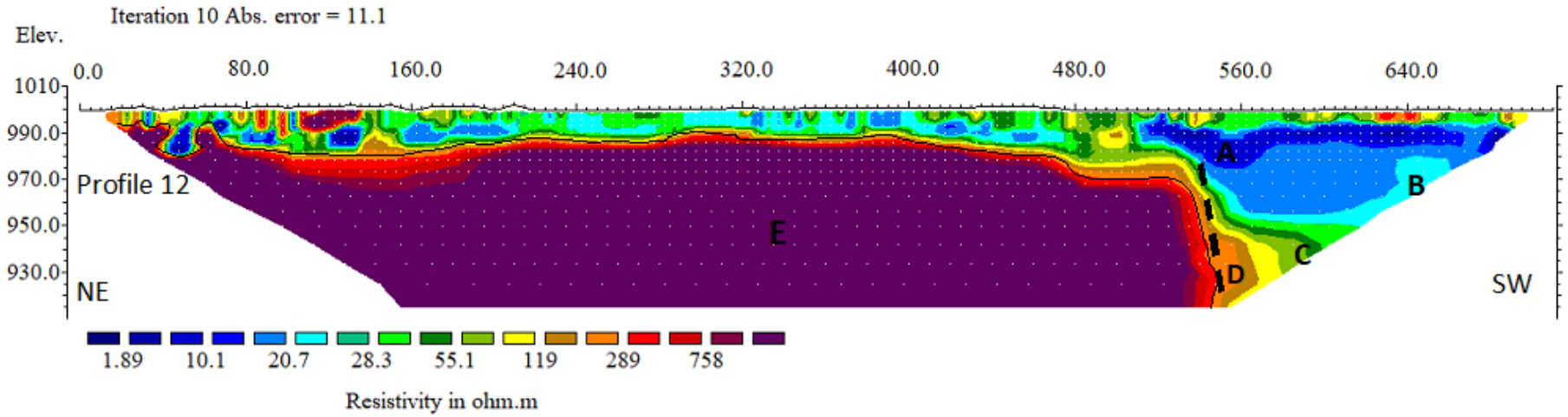


Figure 5. 11: Resistivity section along line 11 situated at y=550 m.

Anomaly A, B and C representing mudstone, sandstone, grey siltstone and coaly material dominate the shallow depth of profile 11. The SW edge of the profile is dominated by anomaly A and B. Also, in this profile the fault anomaly is as presented. There is a clear transition, the NE portion of

the profile is dominated by high resistivity values ρ>28.3 Ωm whilst the SW portion is dominated by only lower resistivity values ρ<28.3 Ωm. Anomaly E dominates the NE portion of the profile from 20m depth to the base of the profile laminated by anomaly D.



Interpretation

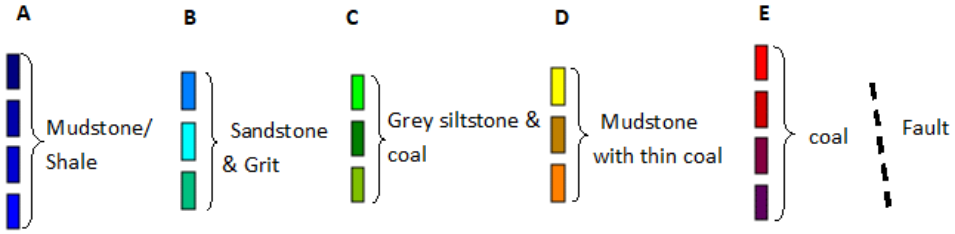
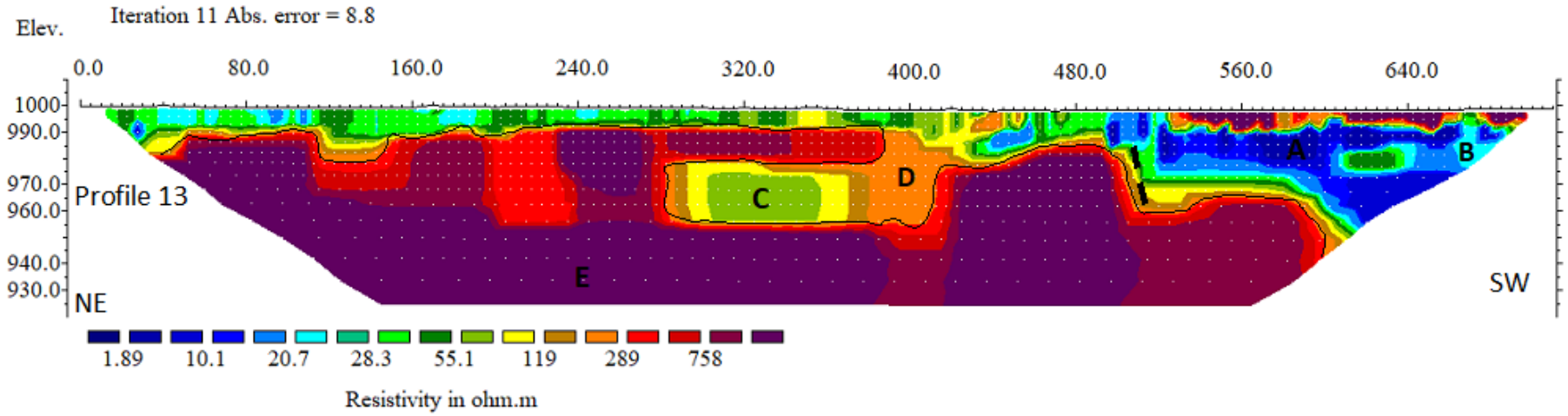


Figure 5. 12: Resistivity section along line 12 situated at y=600 m.

Profile 12 shallow depth comprise of Anomaly B, C, D and E (sandstone, grey siltstone, mudstone and coal). The NE side of the fault anomaly is dominated by high resistivity values ρ>289 Ωm whilst the SW side is dominated by only lower resistivity values ρ<289 Ωm of Anomaly A and B. Anomaly E dominates the NE portion of the profile from 21m depth to the base of the profile and is laminated by anomaly D.



Interpretation

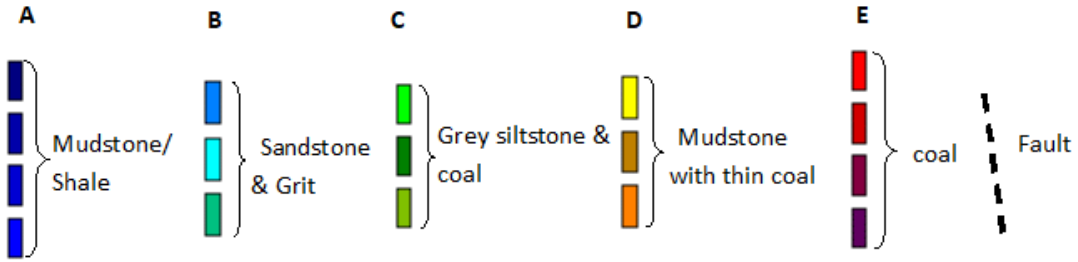
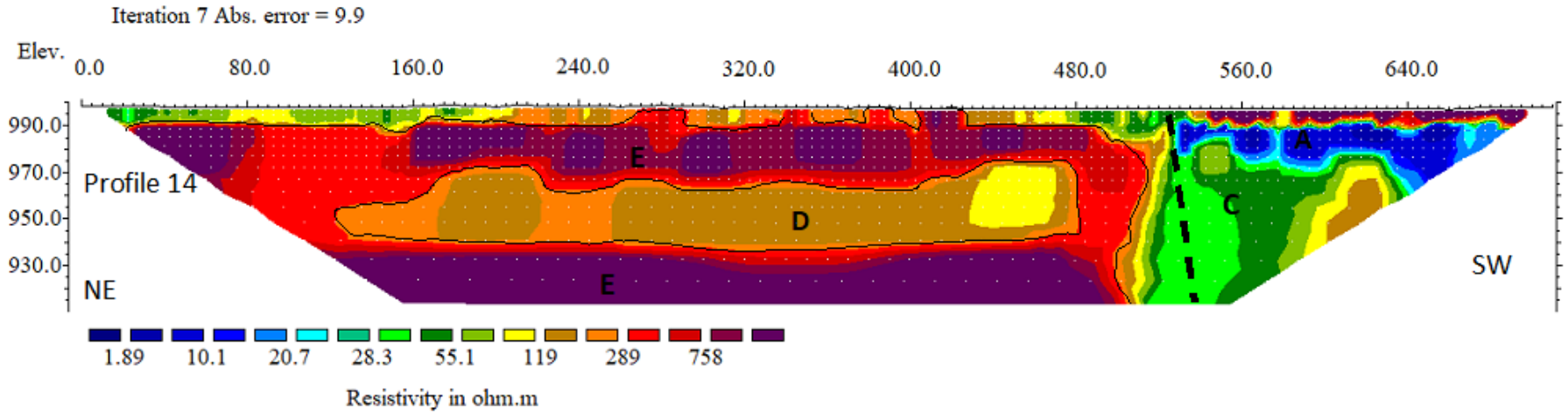


Figure 5. 13: Resistivity section along line 13 situated at y=650 m.

Anomaly E (coal) is the most prominent anomaly in profile 13. The fault anomaly is as presented showing the NE side of the fault anomaly dominated by high resistivity values ρ>289 Ωm whilst the SW side is dominated by lower resistivity values ρ<289 Ωm. The Shallow depth comprise of resistivity ranges for sandstone, grey siltstone, mudstone and coal represented by Anomaly B, C, D and E. A portion in the top SW edge of the profile is dominated by Anomaly A and B.



Interpretation

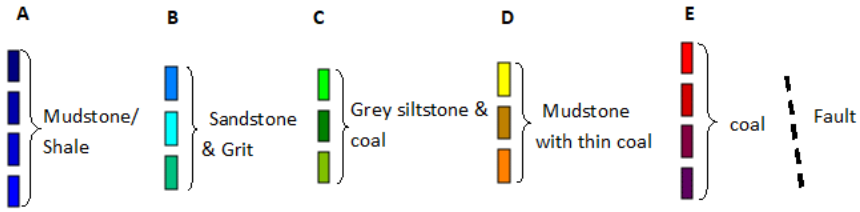


Figure 5. 14: Resistivity section along line 14 situated at y=700 m.

Profile 14 is dominated by high resistivity values. The shallow depths show anomalies C, D, and E representative of grey siltstone, mudstone and coaly material. E is the most prominent anomaly in the profile and shows an interbedded layer of anomaly D. The fault anomaly is as presented with a clear transition, the NE side of the fault anomaly dominated by high resistivity values ρ >119 Ωm whilst the SW side is dominated by only lower resistivity values ρ <119 Ωm.

5.3 Three-dimensional resistivity models

The fourteen ERT 2D profiles were collated using the Res2DInv software. The resulting .dat file was processed using the RES3DINV program to generate eleven horizontal slices representative of the imaged subsurface at different depths (Fig. 5.15). Their depths are 0–3.50, 3.50–7.52, 7.52–12.2, 12.2–17.5, 17.5–23.6, 23.6– 30.6, 30.6–38.7, 38.7–48.0, 48.0–58.8, 58.8–71.1 and 71.1–85.2 m respectively. The same anomaly representations as those used in the 2D profiles were used to characterize the 3D profiles for easy comparison. The low range resistivity values from approximately 1.89>Ωm<10.1 (mudstone/ shale) were assigned anomaly A, ranges from 10.1>Ωm<20.7 were assigned sandstone & grit (anomaly B), grey siltstone and coal were assigned anomaly C with a resistivity range 28.3>Ωm<55.1. Anomaly D represents a range from 119>Ωm<289 representative of mudstone with thin coal and anomaly E represent high resistivity variations values from 289 to >758 Ωm (coal).

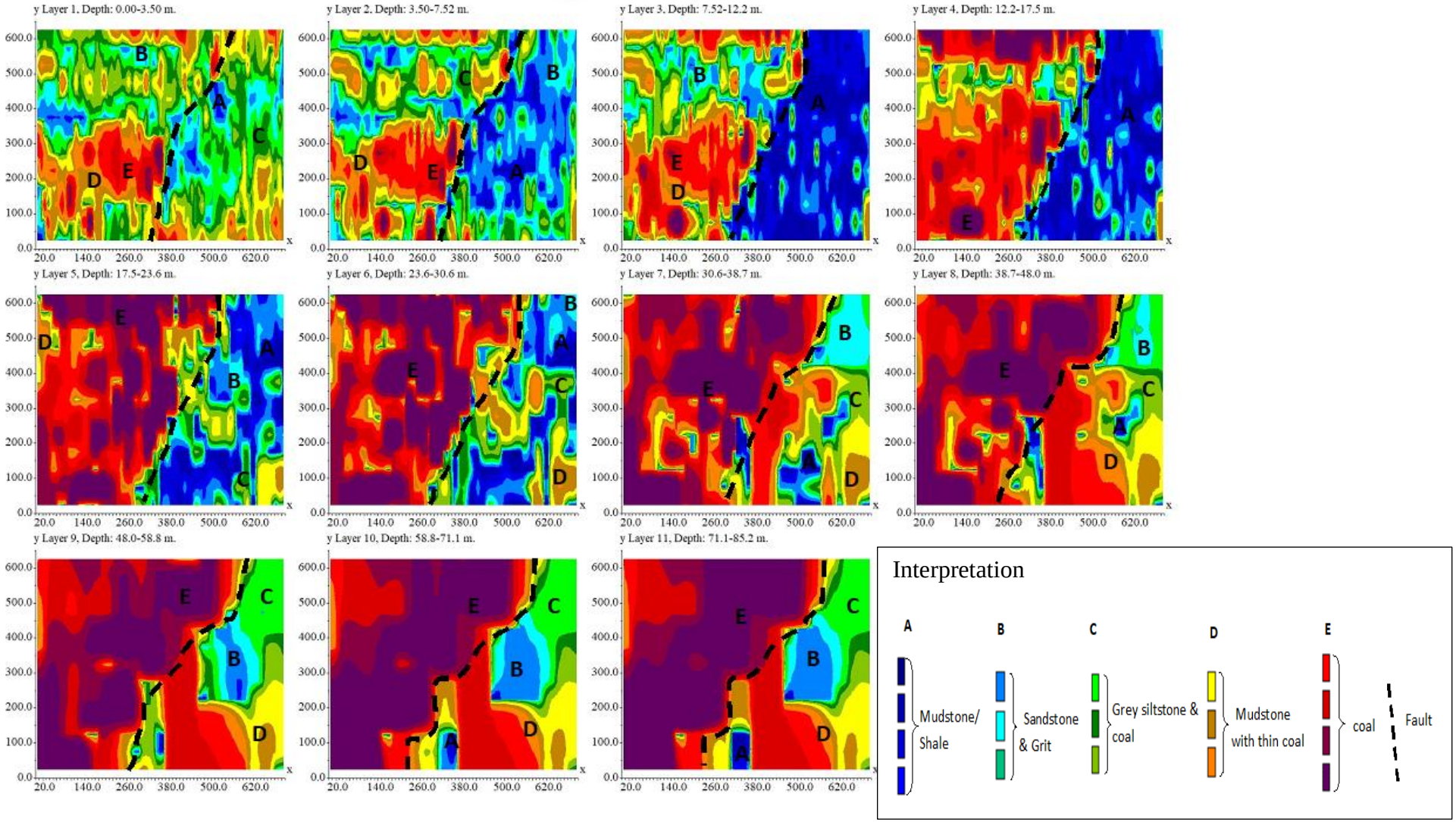


Figure 5. 15: Shows the inversion results (10.9% Root Mean Square) obtained using the Resistivity three dimension inversion (Res3DInv) program

The results show resistivity variation with depth. Layer 1; depth 0–3.50m shows a wide range of resistivities, anomaly A to E (mudstone/shale, sandstone, grey siltstone, mudstone and coal). From Layer 2 (depth; 3.50–7.52m) high resistivity values (ρ>28.3Ωm) are restricted to the NE portion with the SW portion dominated by low resistivity values (ρ< 28.3 Ωm). From layer 3 to layer 5 (depth: 7.52–23.6 m), Anomaly A (mudstones/shale) is dominant in the SW portion with the NE portion characterized by resistivities greater than 20.7 Ωm representative of sandstone, grey siltstone, mudstone and coal. Anomaly E is profound from layer 4 to layer 11 (depth; 12.2-85.2m) restricted only to the NE portion of the profile. From layer 5 (depth; 17.5m), there is a gradual appearance of high resistivity values on the SW portion that was initially dominated by low resistivity values. Reference to the fault anomaly, from layer 2 to layer 6 (depth; 3.50-30.6m) the right side (SW) does not have anomaly E (coal), it only appears from layer 7 (depth; 30.6).

As seen in the 2D profiles, the 3D profiles also show that there is a near surface layer with varied resistivity values, after which the NE portion is gets dominated by high resistivity values compared to the SW portion. This is intimately linked to the distribution and placement of coal seams, in the NE portion they are placed at shallower depth. The coal on the SW portion is from layer 7 (depth; 30.6m), this shows a displacement as the coals in the SW are at deeper depth.

The results corroborate the Res2DINV results as they show the same anomaly trends. Depths near the surface are characterized by varied anomalies (A to E), after which the NE portion is dominated by high resistivity anomalies compared to the SW portion. Reference to the fault anomaly the left (NE) side is characterized by anomalies greater than 289 Ωm, with a dominance of anomaly E (coal) and the right (SW) side with anomalies less than 289 Ωm dominated by anomaly A, B and C (mudstone, sandstone, grey siltstone and coaly material).

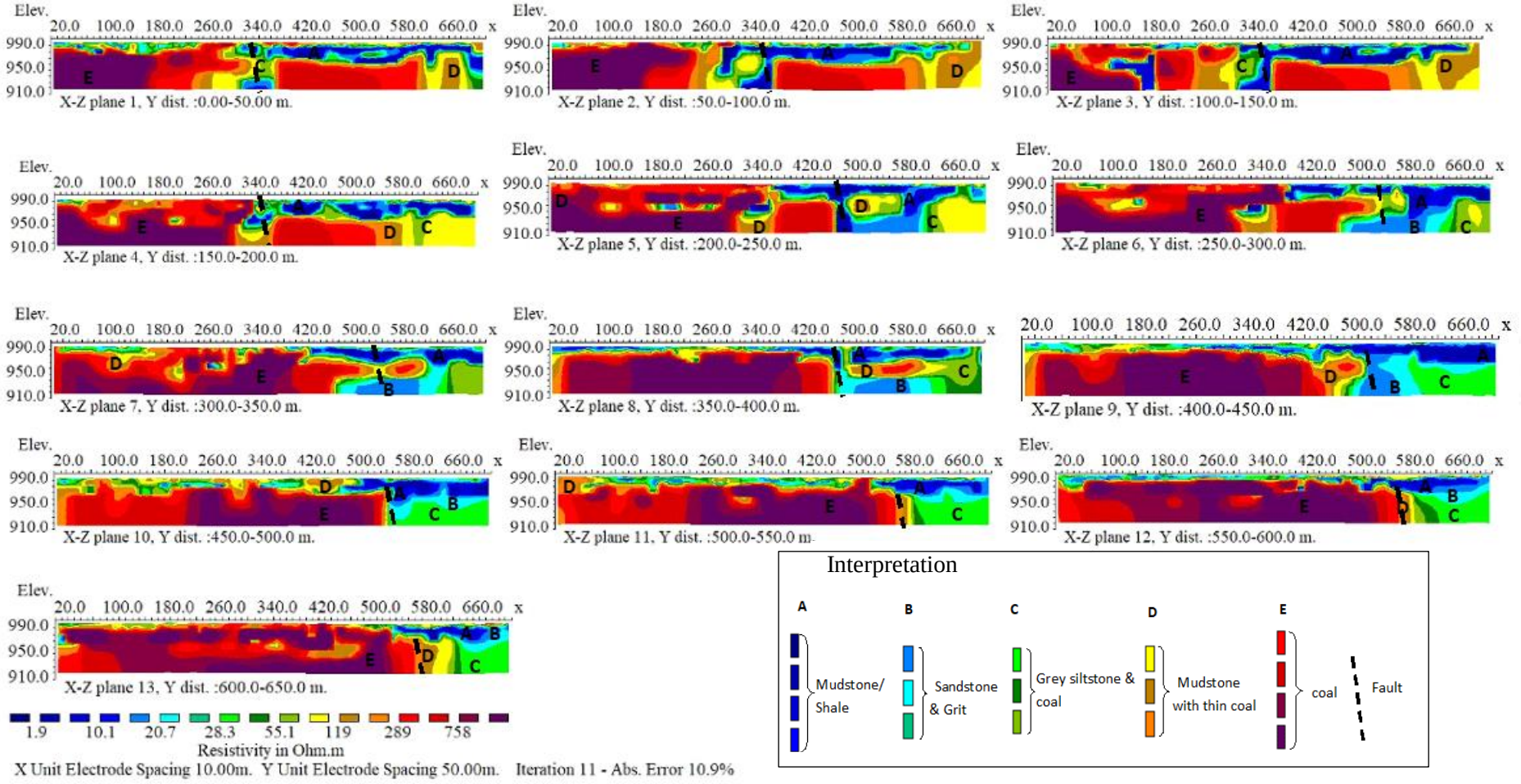


Figure 5. 16: Shows the 3D results in the form of vertical slices obtained also from the inversions carried out using the Res3DInv program

CHAPTER 6- DISCUSSION AND CONCLUSION

6.1 Discussion

A geoelectrical study using the Electrical Resistivity Tomography method was carried out in the Mmamabula area along fourteen equally spaced (50m) ERT survey lines. The lines run approximately NE–SW, more or less perpendicular to an inferred fault location. A dipole-dipole array with electrode spacing of 10m was used. The results and interpretation derived from the 2D and 3D ERT analysis show the inversion model and the geological interpretation.

The 2D models display a variation in the resistivity values in the vertical and horizontal direction, indicating heterogeneity in the subsurface rocks of the Mmamabula area (Nthaba et al., 2020). The profile or depth section, is designed to be consistent with the measurements, and its interpretation is based on the resistivity values and the diagnostic soil and rock's bulk densities (Arjwech et al,. 2020). The resistivity contrast can be used to discriminate between different sedimentary units; e.g. very low resistivity sediments can be differentiated from those with high resistivity. The rocks are differentiated by their electric properties according to their degree of fracturing and lithologies. The rock boundaries shown on the resistivity profiles are based on lithological borehole information available from log B55- fig 2.4b

The colour in the figures represents the resistivity distribution as determined from inversion, and the colour bar (1.89Ωm- 758Ω m) represents the electrical resistivity range for the subsurface materials under study. The presence of distinct resistivity contrasts in the subsurface made it possible to determine the range of the different geo-electric layers hence the designation of the different lithological units. In order to accurately identify the geoelectrical layers (lithological identification), geoelectrical results interpretations were compared with geological drilling data (log B55- fig 2.4b) and the interpretation of the lithology of Mmamabula area by Green (1973).

From the sections, the anomalous regions observed across are designated letters A, B, C and D representative of the following sedimentary units; mudstone/ shale (anomaly A), sandstone & grit (anomaly B), grey siltstone (anomaly C), mudstone with thin coal (anomaly D) and anomaly E representative of coal. Across all the 2D sections; depth near the surface is characterized by low and intermediate resistivity values (anomaly A to D).

Coal as observed, portray high resistivity values relative to other rock units (red and purple colours), it also has a broad range of resistivity values ranging from 288 Ωm to greater than 758 Ωm (anomaly E). This broad range is due to its complexity and the factors affecting its placement. Coal usually has a high resistivity compared to other sedimentary rock units with a wide range of resistivity values as its resistivity is a influenced by degree of metamorphism (or carbonization) mineral composition and petrophysical character (Singh et al.,(2004).

Palacky (1988) suggested that high resistivity values (red colour) are a representation of rocks of superior quality and/ also intact or unweathered rock. This statement also applies to coal ranks; Farag (2005) suggested that weakly metamorphosed coal (moist coal) has resistivity between 10 Ωm and 100 Ωm and that further carbonisation results in the formation of free carbon stringers and a reduction of organic radicals in coal resulting in lower values of resistivity. It should also be noted that the degree of resistivity decrease is dependent on the type of metamorphism. Highly metamorphosed coal, like anthracite, displays relatively low values of resistivity from 0.001 to 10 mm (Farag, 2005).

The adsorption or desorption of gas also has a great influence on the resistivity of coal (Singh et al., 2004). The previous work done by Feng et al., (2018) indicate that the resistivity of gas-containing coal increases linearly as the gas content decreases in desorption and the resistivity decreases as the gas content increases during adsorption. Suggate (1974) also indicated that the coal quality is a function of the depth of its placement, and thus concluded that deep seated coals are of high quality due to burial depth pressures hence show high resistivity values.

The depth of coal seam as identified from the profiles is varies from depth between 5-11 m in the NE side and 37- 46m in the SW side. It is clearly indicative that the NE side has upper seated coals at shallow depth compared to those in the SW side. Two coal seams were delineated in some profiles in the NE side (figure 5.3- 5.7), the thin upper seam and thick underlying seam. The two coal seams are separated by a layer of either grey siltstone with thin coal and /both mudstone with thin coal of variable thickness. Williamson (1996), also noted this interbedding, he suggested that coal seams in Middle Ecca are interbedded with sandstone, siltstone and, or the mudstone sequence.

The remaining profiles (figure 5.1- 5.2 and 5.8- 5.14) show only one thick coal layer in the NE portion contrary to the expected two layers. This is due to the fact that the method used

cannot distinctively and accurately resolve a low resistive layer sandwiched between a highly resistive of coal seams (Green et al., 1988), thus two coal seams separated by a low resistive layer are presented as one thick layer of coal masking the low resistive layer.

A similar approach in delineating coal seams was used by Mohammed et al (2016); he conducted a geoelectrical investigation in Tai Area of Gombe State, North Eastern Nigeria. His main focus was to map the possible location of the coal seam in the area for future exploitation. He targeted the resistivity values associated with the coal seam, the lateral extent of the seam, and also the depth to the seam. The findings revealed coal seams with a resistivity range from approximately 250 Ωm to 900 Ωm at depth varying from 3 m to 17.2 m.

The coal seams in Mmamabula were also studied by Nthaba et al., 2020 using a similar approach as this study. His main focus was on locating and characterizing the coal seams. In his results he revealed two observable coal seams; the shallower coal seam at approximately 13.6 m depth and the underlying seam at approximately 50m and 60m.

Constraints on the geometry of the Mabuane Fault (Fig 5.15) was also achieved using the Electrical Resistivity method. The ERT inversion images provide a resolution that is able to depict a fault plane between contrasting resistivity values of coal and other delineated sedimentary units. The finding of this study reveal a disruption in the sedimentary units. The Law of Lateral Continuity suggests that all rock layers are laterally continuous and can only be broken up or displaced by later events (Davidson, 1965). As stated above, **t**he depth of the coal seams is variable in the NE side compared to the SW side. The displacement of rock units is in most cases a result of faulting as is the case for the referenced coal seams. The black line cutting across the profiles in figures 5.1- 5.4 show an offset between the layers.

The Mabuane fault; as mentioned by Williamson (1996) is a northwest-south east trending fault with a downthrow to the south west that separates the South Central Mmamabula coalfield from the North central Mmamabula coalfield. Smith (1961) also stated that due to the fault, the south western part (known to be the downthrow side of the Mabuane fault) comprise of coals at greater depth. Figure 5.1- 5.4 show this vertical displacement on the coal seams due to the fault.

Results of the 3D profiles generated in this study indicate a clear contact (fig 5.15; Layer 1-6) revealed through the resistivity contrasts (the left side, the NE is dominated high resistivity values compared to the right side (SW)). Resistivity values associated with coal seams are more pronounced from layer 4; depth 12m in the NE side and in the SW side the coals manifest from layer 7: depth 30.6m. Information from the 2D and 3D models developed reveal that the Mmamabula coal seams were affected by vertical displacement (faulting) as the seams have been offset (figure 5.1- 5.4).

Although the application of ERT survey was successful in unravelling the Mmamabula subsurface complexity, ERT has its own limitations. It is unable to provide reliable stand-alone information about subsurface properties from just the inverted electrical conductivity distributions.

The generalizability of the results of this research is restricted by;

- Resolution at depth- the ERT technique is sensitive to some degree, to such variation, particularly as dipole separation increases resolution at depth decreases hence at a depth the characterization of resistivity zones was ambiguous.
- Interpretation of low resistivity zones at depth; it is challenging because the zones become wider at depth (Ganerød et al., 2006)

6.2 Conclusion

The multi-electrode Electrical Resistivity method was applied in this study to generate 2D and 3D high resolution images of the subsurface resistivity variation in part of Mmamabula area. The purpose of the research was to understand the subsurface placement of coal seams and the influence of geological structures on coal seam placement. The utility of the method approach lies in its ability to differentiate a sedimentary unit as a distinct resistivity zone. Dipole-dipole was used as it is mostly sensitive to horizontal variations in the substratum. A roll along technique was deployed to extend the system length from 480m to 720m to cover the survey line length.

Results from the fourteen (14) electrical reisitivity survey lines acquired in the study area and their interpretation indicates that the geological setting of the study area varies considerably. Both the 2D and 3D sections show a heterogeneous subsurface comprising of the following lithologies; mudstone/ shale, sandstone & grit, grey siltstone, mudstone and

coal. Coal placement is delineated at variable depths at approximately 5-11 m in the NE side and 37- 46m in the SW side indicating that the coals in the NE side are at shallow depth contrary to those in the SW side.

- Using the results from interpretation and analysis of the resistivity profiles obtained from the inversion of ERT dataset, it was possible to infer the presence and location of the Mabuane fault. The fault anomaly is between contrasting resistivity values of coal and other delineated sedimentary units and is observed through both the 2D and 3D ERT profiles.
- The coal distribution as seen from the 3D profiles is from variable depths; the NE side coal seams are from depth 12m and 30.6 m in the SW side.
- Fig 5.1-5.4 show a vertical displacement of the coal seams.
- Due to the disruption in the lateral extent of the seams it can be inferred that the faulting observed is post-depositional.

This study shows that ERT can be used in the study of near-surface geological structures i.e. faults and mapping of coal deposits. The method can also be applied to study tectonic features, their areal extent as well as confirm their depth and is convenient to use for assessment of large-scale fault structures.

REFERENCES

Al-Amoush, H., & Rajab, J. A. (2018). The use of Electrical Resistivity Tomography to investigate basaltic lava tunnel based on the case study of Al-Badia cave in Jordan. *Indonesian Journal on Geoscience, 5(2), 161-177.*

Al-amoush, H., Rajab, J. A., & Al-tarazi, E. (2017). Electrical Resistivity Tomography modeling of vertical lithological contact using different electrode configurations. *Jordan Journal of Earth and Environmental Sciences, 8, 27-34.*

Aizebeokhai, A. P. (2010). 2D and 3D geoelectrical resistivity imaging: Theory and field design. *Scientific Research and Essays, 5(23), 3592-3605.*

Amalina, M. N., Nordiana, M. M., Bery, A. A., bin Anuar, M. N. A., Maslinda, U., Sulaiman, N., Saharudin, M. A., Hishan, H., Nordiana, A. N., Taqiuddin, Z. M. (2017). Application of 2-D Resistivity Imaging and Seismic Refraction method in identifying the structural geological contact of sedimentary lithologies. In *IOP Conference Series: Earth and Environmental Science, 62, 012005*.

Ball, L. B., Kress, W. H., Anderson, E. D., Teeple, A. P., Ferguson, J. W., & Colbert, C. R. (2004). Surface geophysical investigation of the areal and vertical extent of metallic waste at the former Tyson Valley Powder Farm near Eureka, Missouri, Spring 2004. *Scientific Investigation Report 2004-5208*.

Barbolini, N. (2010). Palynology of a coal seam in Karoo deposits of Botswana and correlation with southern African coal-bearing strata. *Doctoral thesis, University of Witwatersrand, South Africa.*

Pierce, K. S., Liechty, D. J., Rittgers, J. B. (2012). Geophysical Investigations Electrical Resistivity Surveys: Santee Basin Aquifer Recharge Study, Santee, California. *Technical Memorandum No. TM-86-68330-2012-23.*

Bennett, J. D. (1989). Review of Lower Karoo coal basins and coal resource development in parts of central and southern Africa with particular reference to northern Malawi. *British Geological Survey*.

Bernard, J., Leite, O., Vermeersch, F., Instruments, I. R. I. S., & Orleans, F. (2006). Multi-

electrode resistivity imaging for environmental and mining applications. *IRIS Instruments, Orleans, France.*

Barbolini, N. (2010). *Palynology of a coal seam in Karoo deposits of Botswana and correlation with southern African coal-bearing strata* (Doctoral dissertation).

Carney, J.N., Aldiss, D.T., Lock, N.P. (1994). *The geology of Botswana*. Geological Survey of Botswana Bulletin, 37, 113pp.

Clark, G. C., Lock, N. P., Smith, R. A., (1986). Coal resources of Botswana. In: Anhaeusser, C. R. and Maske, S. (eds.). Mineral deposits of Southern Africa. *Geological Society of South Africa, Johannesburg, 2071-2085.*

Dahlin, T. (2001). The development of DC resistivity imaging techniques. *Computers & Geosciences, 27(9), 1019-1029.*

Dahlin, T., & Zhou, B. (2006). Multiple-gradient array measurements for multichannel 2D resistivity imaging. *Near Surface Geophysics, 4(2), 113–123.*

Degnan, J. R., Moore, R. B., & Mack, T. J. (2001). Geophysical investigations of well fields to characterize fractured-bedrock aquifers in Southern New Hampshire.*US Geological Survey, Water-Resources Investigation Report 2001-418.*

Diaferia, I., Barchi, M., Loddo, M., Schiavone, D., & Siniscalchi, A. (2006). Detailed imaging of tectonic structures by multiscale Earth resistivity tomographies: The Colfiorito normal faults (central Italy). *Geophysical research letters*, *33*(9).

Edwards, L. S. (1977), A modified pseudosection for resistivity and induced-polarization, *Geophysics, 42,* 1020–1036.

Farag, K. S. (2005). Multi-dimensional resistivity models of the shallow coal seams at the opencast mine 'Garzweiler I'(northwest of Cologne) inferred from radiomagnetotelluric, transient electromagnetic and laboratory data. *Doktorarbeit, Institut für Geophysik und Meteorologie, Universität zu Köln, Cologne, Germany*.

Fazzito, S., Rapalini, A., Cortés, J.M., (2006). *Tomografía geoeléctrica en zonas de fallas cuaternarias: dos ejemplos en la Precordillera centro-occidental de Mendoza, Revista de la Asociación Geológica Argentina, Serie D,* Publicación Especial, pp. 41–47

Feng, Z., Wang, C., Dong, D., Zhao, D., & Zhou, D. (2018). Experimental study of the characteristic changes of coal resistivity during the gas adsorption/desorption process. *Advances in Materials Science and Engineering*, *18*.

Gélis, C., Revil, A., Cushing, M. E., Jougnot, D., Lemeille, F., Cabrera, J., ... & Rocher, M. (2010). Potential of electrical resistivity tomography to detect fault zones in limestone and argillaceous formations in the experimental platform of Tournemire, France. *Pure and Applied Geophysics*, *167*(11), 1405-1418.

Ganerød, G. V., Rønning, J. S., Dalsegg, E., Elvebakk, H., Holmøy, K., Nilsen, B., & Braathen, A. (2006). Comparison of geophysical methods for sub-surface mapping of faults and fracture zones in a section of the Viggja road tunnel, Norway. *Bulletin of Engineering Geology and the Environment*, *65*(3), 231.

Giocoli, A., Galli, P., Giaccio, B., Lapenna, V., Messina, P., Peronace, E., ... & Piscitelli, S. (2011). Electrical resistivity tomography across the Paganica-San Demetrio fault system (L'Aquila 2009 earthquake). *Bollettino di Geofisica Teorica ed Applicata*, *52*(3), 457-469.

Giocoli, A., Magrì, C., Vannoli, P., Piscitelli, S., Rizzo, E., Siniscalchi, A., ... & Di Nocera, S. (2008). Electrical resistivity tomography investigations in the ufita Valley (southern Italy). *Annals of Geophysics*.

Green, D., 1961. *The Mamabule Coal Area*. vol. 2. Geological Survey Department, Bechuanaland Protectorate, pp. 1–65.

Green D. (1966). *The Karroo system in Bechuanaland*, Bulletin of the Geological Society of Bechuanaland n2, Gaborone. 74pp.

Green, D.H., Fenton, M.M., Sterenberg, C., Sartorelli, T., Henderson, J., Pesowski, M., (1988). *Surface Geophysical Coal Research Project 1984 to 1986*. Final Rep., vol. 112, 148p.

Griffiths, D. H., & Barker, R. D. (1993). Two-dimensional resistivity imaging and modelling in areas of complex geology. *Journal of applied Geophysics*, *29*(3-4), 211-226.

Griffiths, D. H., Turnbull, J., & Olayinka, A. I. (1990). Two-dimensional resistivity mapping with a computer-controlled array. *First break*, *8*(4).

Hasan, M., Shang, Y. J., Jin, W. J., & Akhter, G. (2019). Investigation of fractured rock aquifer in South China using electrical resistivity tomography and self-potential methods. *Journal of Mountain Science*, *16*(4), 850-869.

Hancox, P. J. (2016). The coalfields of South-Central Africa: A current perspective. *Episodes*, *39*(2), 407-428.

Herman, R. (2001). An introduction to electrical resistivity in geophysics. *American Journal of Physics*, *69*(9), 943-952.

Instruments, I. R. I. S. (2005). Syscal Pro User's manual.

Ismael, M., & Shariah, A. (2019). *Application of Electrical Resistivity Tomography Synthetic Modeling*. *24*, 931–948.

Iungu, W. G. (2015). *Application of 2d electrical resistivity tomography to assess the influence of geology and geological structures on groundwater occurrence and potential in Konza area, Kenya* (Doctoral dissertation, University of Nairobi).

Ji, H. G., Ma, H. S., Wang, J. A., Zhang, Y. H., & Cao, H. (2012). Mining disturbance effect and mining arrangements analysis of near-fault mining in high tectonic stress region. *Safety science*, *50*(4), 649-654.

Kecojevic, V., Willis, D., Wilkinson, W., & Schissler, A. (2005). Computer mapping of faults in coal mining. *International Journal of Coal Geology*, *64*(1-2), 79-84.

Keller, G. V. (1982). *Electrical properties of rocks and minerals*. Handbook of physical properties of rocks.

Kong, P., Jiang, L., Shu, J., & Wang, L. (2019). Mining Stress Distribution and Fault-Slip Behavior: A Case Study of Fault-Influenced Longwall Coal Mining. *Energies*, *12*(13), 2494.

Kress, W. H., & Teeple, A. P. (2005). *Two-Dimensional Resistivity Investigation of the North Cavalcade Street Site, Houston, Texas, August 2003*. US Department of the

Interior, US Geological Survey.

Loke, M. H. (1999). Electrical imaging surveys for environmental and engineering studies. *A practical guide to*, *2*.

Loke, M. H. (2000). Topographic modelling in resistivity imaging inversion. In *62nd EAGE Conference & Technical Exhibition Extended Abstracts, D-2*.

Loke, M. H. (2001). Tutorial: 2-D and 3-D electrical imaging surveys, 128 p. *Geotomo Software, Malaysia*.

Loke, M. H., Acworth, I., & Dahlin, T. (2003). A comparison of smooth and blocky inversion methods in 2D electrical imaging surveys. *Exploration geophysics*, *34*(3), 182-187.

Loke, M. H. (2004). Tutorial: 2-D and 3-D electrical imaging surveys.

Loke, M.H., 2014. Tutorial: 2-D and 3-D electrical Imaging Surveys, Malaysia. Geotomo Software

Lowrie, W. (2007). *Fundamentals of geophysics*. Cambridge university press. Maganti,

Mohammed, M. A., Adewumi, T., Ahmed, A. L., & Lawal, K. M. (2016). Electrical Resistivity Imaging of a Coal Deposit at Tai Area of Gombe State, North Eastern Nigeria. *Journal of Environmental and Earth Science*, *6*(6), 55.

Mojica, A., Pérez, T., Toral, J., Miranda, R., Franceschi, P., Calderón, C., & Vergara, F. (2017). Shallow electrical resistivity imaging of the Limón fault, Chagres River Watershed, Panama Canal. *Journal of Applied Geophysics*, *138*, 135-142.

Molinda, M., & Ingram, D. K. (1990). Effects of structural faults on ground control in selected coal mines in southwest Virginia. *International Journal of Mining and Geological Engineering*, *8*(4), 332-347.

Monahan, S. M. (2013). Investigating fault structure using electrical resistivity tomography.

Nelson, W. J. (1981). Faults and their effect on coal mining in Illinois. *Circular no. 523*.

Nthaba, B. (2017). Investigation of Lotsane earth fill dam for internal defects using time-

lapse electrical resistivity imaging and frequency domain electromagnetic methods.

Nthaba, B., Shemang, E., Hengari, A., Kgosidintsi, B., & Tsuji, T. (2020). Characterizing coal seams hosted in Mmamabula Coalfield, central Botswana using pseudo-3D electrical resistivity imaging technique. *Journal of African Earth Sciences*, 103866.

Omowumi, F. P., Abiola, O., & Festus, F. O. (2018). *Application of Electrical Resistivity Imaging in investigation of Late Maastrichtian coal seam at Amoso Edda / Owutu Edda environs , Anambra Basin , Nigeria*. (January), 32–39.

Palacky, G. J. (1988). Resistivity characteristics of geologic targets. *Electromagnetic methods in applied geophysics*, *1*, 53-129.

Phengnaone, K., Arjwech, R., & Everett, M. (2020). 2D electrical resistivity tomography (ERT) method to delineate coal seams: Case studies on lignite and anthracite. *Songklanakarin Journal of Science & Technology*, *42*(4).

Qarqori, K., Rouai, M., Moreau, F., Saracco, G., Dauteuil, O., Hermitte, D., ... & Le Carlier de Veslud, C. (2012). Geoelectrical tomography investigating and modeling of fractures network around Bittit Spring (Middle Atlas, Morocco). *International Journal of Geophysics*, *2012*.

Racic, L., & Millis, T. (2006). Mapping the subsurface for mineral exploration. *first break*, *24*(7).

Ramachandran, K., Tapp, B., Rigsby, T., & Lewallen, E. (2012). Imaging of fault and fracture controls in the Arbuckle-Simpson aquifer, southern Oklahoma, USA, through electrical resistivity sounding and tomography methods. *International Journal of Geophysics, 2012.*

Robert, T., Caterina, D., Deceuster, J., Kaufmann, O., & Nguyen, F. (2012). A salt tracer test monitored with surface ERT to detect preferential flow and transport paths in fractured/karstified limestones. *Geophysics*, *77*(2), B55-B67.

Samanlangi, A. I. (2018). Coal Layer Identification using Electrical Resistivity Imaging Method in Sinjai Area South Sulawesi. In *Journal of Physics: Conference Series* (Vol. 979). IOP Publishing.

Schmidt, A. (2008). Electrical and magnetic methods in archaeological prospection. In *Seeing the unseen. Geophysics and landscape archaeology* (pp. 93-108). CRC Press.

Segwabe, T. (2009). *The geological framework and depositional environments of the coal-bearing Karoo Strata in the Central Kalahari Karoo Basin, Botswana* (Doctoral dissertation, Rhodes University). Bulletin 26, Geological Survey, Botswana,

Singh, K. K. K., Singh, K. B., Lokhande, R. D., & Prakash, A. (2004). Multielectrode resistivity imaging technique for the study of coal seam.

Smith, R.A. (1984). *The lithostratigraphy of the Karoo Supergroup in Botswana. Bulletin Geological Survey Botswana*, 26. 239p.

Silvester, P.P., Ferrari, R.L., (1990). *Finite Elements for Electrical Engineers*. Cambridge University.

Sjödahl, P., (2006). *Resistivity Investigation and Monitoring for Detection of Internal Erosion and Anomalous Seepage in Embankment Dams* (Doctoral Thesis). Lund University, Sweden, pp. 86p.

Sjödahl, P., Dahlin, T., Johansson, S., & Loke, M. H. (2008). Resistivity monitoring for leakage and internal erosion detection at Hällby embankment dam. *Journal of Applied Geophysics*, *65*(3-4), 155-164.

Spiegel, R. J., Sturdivant, V. R., & Owen, T. E. (1980). Modelling resistivity anomalies from localized voids under irregular terrain. *Geophysics*, *45*(7), 1164-1183.

Štěpančíková, P., Dohnal, J., Pánek, T., Łój, M., Smolková, V., & Šilhán, K. (2011). The application of electrical resistivity tomography and gravimetric survey as useful tools in an active tectonics study of the Sudetic Marginal Fault (Bohemian Massif, central Europe). *Journal of Applied Geophysics*, *74*(1), 69-80.

Telford, W.M., Geldart, L.P., Sheriff, R.E., (1990). *Applied Geophysics*, second ed. Cambridge University Press, Cambridge, UK. 790p

Torgashov, E. V., Anderson, N. L., & Kovin, O. (2010). Fault Detection Using Electrical Resistivity Tomography. In *23rd EEGS Symposium on the Application of Geophysics*

to Engineering and Environmental Problems (pp. cp-175). European Association of Geoscientists & Engineers.

Van Schoor, M., & Fourie, C. J. S. (2014). The application of geophysics in South African coal mining and exploration. *Journal of the Southern African Institute of Mining and Metallurgy*, *114*(10), 875-879.

Vanneste, K., Verbeeck, K., & Petermans, T. (2008). Pseudo-3D imaging of a low-slip-rate, active normal fault using shallow geophysical methods: The Geleen fault in the Belgian Maas River valley Imaging a slow active normal fault in 3D. *Geophysics*, *73*(1), B1-B9.

Williamson, I.T., (1996). *The geology of the area around Mmamabula and Dibete: including an account of the Greater Mmamabula Coalfield*. Geol. Surv. Dep. Minist. Nat. Resour. Water Aff. Repub. Botsw. 6, 239p.

Zhou, B., & Dahlin, T. (2003). Properties and effects of measurement errors on 2D resistivity imaging surveying. *Near surface geophysics*, *1*(3), 105-117.